Supercond. Sci. Technol. **15** (2002) 991–1010 PII: S0953-2048(02)32090-6

The strain and temperature scaling law for the critical current density of a jelly-roll Nb_3Al strand in high magnetic fields

Simon A Keys[1], **Norikiyo Koizumi**[2] **and Damian P Hampshire**[1]

[1] Department of Physics, Superconductivity Group, University of Durham, South Road, Durham, DH1 3LE, UK

[2] Superconducting Magnet Laboratory, JAERI, 801-1 Mukoyama, Naka-machi, Naka-gun, Ibaraki-ken, 311-0193, Japan

E-mail: d.p.hampshire@durham.ac.uk

Received 19 December 2001, in final form 12 March 2002
Published 10 May 2002
Online at stacks.iop.org/SUST/15/991

Abstract

The engineering critical current density (J_E) and the index of transition, N (where $E = \alpha J^N$), of a Nb_3Al multifilamentary strand, mass-produced as a part of the Fusion programme, have been characterized as a function of field (B), temperature (T) and strain (ε) in the ranges $B \leqslant 15$ T, $4.2\ \mathrm{K} \leqslant T \leqslant 16$ K and $-1.79\% \leqslant \varepsilon \leqslant +0.67\%$. Complementary resistivity measurements were taken to determine the upper critical field ($B_{C2}(T, \varepsilon)$) and the critical temperature ($T_C(\varepsilon)$) directly. The upper critical field defined at $5\%\rho_N$, $50\%\rho_N$ or $95\%\rho_N$, is described by the empirical relation $B_{C2}^{\rho_N}(T, \varepsilon) = B_{C2}^{\rho_N}(0, \varepsilon)\left[1 - \left(T/T_C^{\rho_N}(\varepsilon)\right)^{\nu}\right]$. The upper critical field at zero Kelvin and the critical temperature are linearly related where $B_{C2}^{\rho_N}(0, \varepsilon) \approx 3.6T_C^{\rho_N}(\varepsilon) - 29.9$, although strictly $B_{C2}^{\rho_N}(0, \varepsilon)$ is a double-valued function of $T_C^{\rho_N}(\varepsilon)$. J_E was confirmed to be reversible at least in the range $-0.23\% < \varepsilon < 0.67\%$. The J_E data have been parameterized using the volume pinning force (F_P) where $F_P = J_E \times B = A(\varepsilon)B_{C2}^{n}(T, \varepsilon)b^p(1 - b)^q$ and $b = B/B_{C2}(T, \varepsilon)$. $A(\varepsilon)$ is taken to be a function of strain otherwise the maximum value of F_P (found by varying the field) was a double-valued function of B_{C2} when the temperature was fixed and the strain varied. To achieve a very high accuracy for the parameterization required by magnet engineers (~1 A), the data were divided into three temperature–strain ranges, $B_{C2}(T, \varepsilon)$ described by the empirical relation and the constants p, q, n and ν and the strain-dependent variables $A(\varepsilon)$, $B_{C2}(0, \varepsilon)$ and $T_C(\varepsilon)$ treated as free-parameters and determined in each range. A single scaling law that describes most of the J_E data has also been found by constraining $B_{C2}(T, \varepsilon)$ using the resistivity data at $5\%\rho_N$ where $\nu = 1.25$, $n = 2.18$, $p = 0.39$ and $q = 2.16$. When $B_{C2}(T, \varepsilon)$ is constrained at $50\%\rho_N$ or $95\%\rho_N$, the scaling law breaks down such that p and q are strong functions of temperature and q is also a strong function of strain. Good scaling provides support for identifying $B_{C2}^{5\%\rho_N}(T, \varepsilon)$ as the characteristic (or average) upper critical field of the bulk material. The J_E data are also consistent with a scaling law that incorporates fundamental constants alone, of the Kramer-like form

$$F_P = \frac{1}{249}\frac{[B_{C2}(T,\varepsilon)]^{\frac{5}{2}}}{(2\pi\Phi_0)^{\frac{1}{2}}\mu_0\kappa^2(T,\varepsilon)}b^{\frac{1}{2}}(1-b)^2,$$

where the Ginzburg–Landau (GL) parameter κ is given by the relation

$$\kappa(T,\varepsilon) = 924\frac{B_{C2}(T,\varepsilon)}{\gamma^{\frac{1}{2}}(\varepsilon)T_C(\varepsilon)(1-t^2)},$$

γ is the Sommerfeld constant and $t = T/T_C(\varepsilon)$. At an applied field equal to the upper critical field found from fitting the Kramer dependence (i.e. at $B_{C2}(T,\varepsilon)$), the critical current is non-zero and we suggest that the current flow is percolative. The functional form of F_P implies that in high fields the grain boundary pinning does not limit J_E, this is consistent with J_E-microstructure correlations in other superconducting materials.

1. Introduction

At present, Nb_3Sn conductors are the materials of choice for high-field applications above 12 T. Although it has been long understood that stoichiometric Nb_3Al and $Nb_3(AlX)$ (X = Ge or Cu) have superior critical temperature (T_C) and upper critical field (B_{C2}) to Nb_3Sn [1–5], only recently have fabrication techniques improved sufficiently for Nb_3Al to emerge as a practical alternative to Nb_3Sn. Nb_3Al conductors offer the potential for less sensitivity to stress (the Young's modulus is about a factor of 2 higher), strain [6–11] and have similar sensitivity to neutron irradiation [12]. Long lengths of the Nb_3Al conductor investigated in this work have been developed, mass-produced and supplied by the Japanese Atomic Energy Research Institute (JAERI) within the framework of the International Thermonuclear Experimental Reactor Engineering Fusion Design Activity (ITER-EFDA) [13, 14]. The conductor contains off-stoichiometric Nb_3Al with slightly lower critical parameters than Nb_3Sn. Nevertheless, because strain tolerance is at a premium in large-scale systems (particularly if they are fabricated using react-and-wind techniques [15]), the engineering critical current density (J_E: the critical current (I_C) divided by the entire cross-sectional area of the wire of diameter 0.81 mm) is now sufficiently high to make the strand a candidate for large-scale fusion systems.

To properly optimize the design of high-field magnet systems, the strain tolerance of the conductor must be known. Large Lorentz forces strain the conductor when the system is energized as does the differential thermal compression between component parts of the strand and/or cable on cooling it to cryogenic temperatures. In most of literature on the strain tolerance of technological conductors, the sample is measured when immersed in a cryogenic liquid including the work on Nb_3Sn [16], NbTi [17, 18], $PbMo_6S_8$ [19, 20], YBCO [21] and BiSCCO [22–25]. However, with the increasing importance of cryocooled and cable-in-conduit systems which operate over a range of temperatures, design engineers need to know how the strain tolerance of conductors in high fields changes as a function of temperature. Such combined variable-temperature, variable-strain measurements of $J_E(B,T,\varepsilon)$ have been reported for Nb_3Sn [26, 28] and recently proven useful in providing a unified scaling law for $J_E(B,T,\varepsilon)$ in a small diameter (0.3 mm) Nb_3Sn wire [7, 8]. Measurements on Nb_3Al are less extensive. High-field variable-temperature data (at constant strain) [29–31] or variable-strain data (at constant temperature) [10, 11] have been reported. To the authors' knowledge, this is the first report of detailed $J_E(B,T,\varepsilon)$ data for a technological Nb_3Al conductor.

The critical science that underpins J_E in bulk polycrystalline A15 superconducting materials such as Nb_3Sn and Nb_3Al is still not properly understood. The semi-empirical Fietz–Webb [32] scaling law for the pinning force, $F_p = J_E \times B = A[B_{C2}(T)]^n b^p(1-b)^q$ where p and q are constants, has proven useful to parameterize J_E data. However the free parameters are strongly correlated. Although the distribution of B_{C2} in bulk A15 materials is much smaller than that of the highly anisotropic high-temperature superconductors [33], the data presented in this work show that a change in B_{C2} of only 1 T can cause p and q to double! In the literature, there have broadly been three approaches to break the correlation, in part driven by the experimental challenges of the measurements. Firstly, p and q have been constrained at the Kramer values [34] $p = 0.5$ and $q = 2$. This widely used approach has been successfully used to parameterize both the variable-temperature and the variable-strain data on technological Nb_3Sn and Nb_3Al conductors where B_{C2} is typically 25–30 T [27, 28, 35–39]. However, because this approach ignores the low J_E data at the highest fields (i.e. the high-field tail), it is not clear to what degree this parameterization is valid or unique. Secondly, resistivity measurements have been used to measure $T_C^{\rho}(\varepsilon)$ and $B_{C2}^{\rho}(T,\varepsilon)$ directly and p and q treated as free parameters to describe the J_E data [26, 31]. Detailed measurements have been reported on a high bronze–Nb_3Sn model monofilament at high temperatures where B_{C2} is relatively low. Whether this approach can be used for technological conductors is to be addressed in this work. Thirdly, all possible values of p and q are considered. Usually, J_E data are measured over as broad a field range and as close to B_{C2} as possible and then fitted [7, 16]. This generally provides an accurate parameterization of the high-field tail. However, it is unclear how to interpret the non-half-integral values of p and q or to what degree the parameterization is unique. In the work presented here, a comparison between these different approaches is provided and their relative merits are discussed.

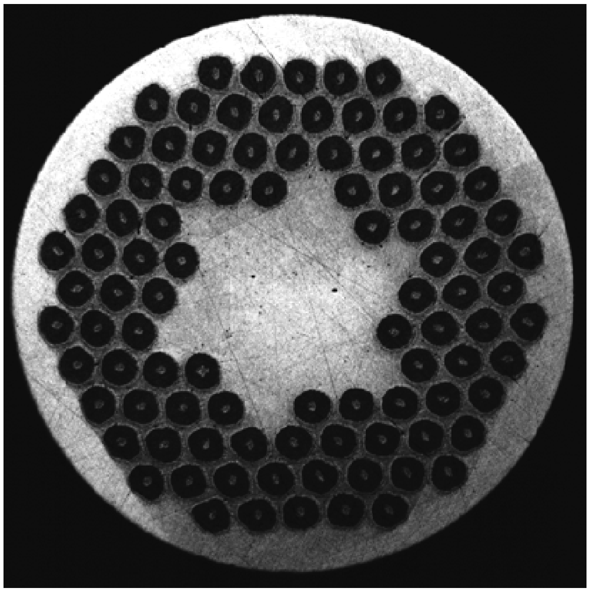

Figure 1. Cross-sectional view of the Nb_3Al strand [13, 42].

Engineering critical current measurements and complementary resistivity measurements as a function of magnetic field, temperature and strain are presented in this paper on a technological Nb_3Al strand. Section 2 presents the experimental procedure used to prepare and measure the Nb_3Al strands. Improved temperature control allows the measurements to be performed up to 200 A at 4.2 K, and 80 A at temperatures above 4.2 K to a stability of ± 5 mK, with an overall uncertainty in temperature of 100 mK. Improvements in the electric field sensitivity resulting in a typical noise level of $\pm 1\ \mu\mathrm{V\ m^{-1}}$ allow reliable measurements of the index, N, of the E–J transition (where $E = \alpha J^N$). The strain range is from -1.79% to 0.67% provided by a helical bending spring [36, 40], rather than free-standing axial tension measurements [16, 41], so large compressive strains can be applied to vary the fundamental properties and test for scaling of J_E in the conductor over as wide a range as possible. The results from these measurements are presented in section 3 along with a comparison with other data in the literature. Three different approaches have been taken to analyse the data. Initially, a technological fit that includes part of the high-field tail is presented in section 4. This accurately parameterizes the critical current data above 1 A and is useful for high-field applications such as the ITER coils. Secondly, a single unified temperature and strain scaling law of the Fietz–Webb form [32] is presented in section 5, which includes a self-consistent interpretation of the tail and can be used to address the underlying mechanism that determines J_E. Thirdly, a scaling law that explicitly includes the Ginzburg–Landau parameter (κ) is considered. Although κ is not measured directly in transport measurements, it must be included in any complete description of scaling. A discussion of this work is presented in section 6 with the summary and conclusions in section 7.

2. Experimental details

2.1. Sample preparation

The strands measured in this study were Sumitomo Cr-plated jelly-roll Nb_3Al strands of 0.81 mm diameter [13, 42]. The strands contain 96 filaments of 54 μm diameter and have a Cu to non-Cu ratio of 1.4. A micrograph of the cross-section of the strand is shown in figure 1. The strands were heat-treated in a high homogeneity furnace at 750 °C for 50 h. This reaction was performed in a high purity argon atmosphere with the samples mounted on a stainless steel (type 316) mandrel. Temperature was monitored during the reaction using a compensated Type N thermocouple that provided an estimated accuracy of ± 4 °C.

Electrical transport measurements were made using a copper beryllium spring sample holder. In order that the strand could be soldered to the CuBe spring, the chrome plating was removed from the strand by etching in an ultrasonic HCl bath for approximately 3 h. The sample was then carefully transferred onto the CuBe spring using a jig. The surface of the spring was then partially electroplated with copper using a copper sulfate/sulfuric acid bath. This closed up any gaps between the strand and the spring and provided a current shunt to protect the strand from burn-out during critical current testing. Typically, a current of 180 mA for 20 h deposited sufficient copper. Finally, the sample was soldered to the spring and current leads and voltage taps attached.

2.2. Measurement procedure

2.2.1. Experimental apparatus. Critical current ($I_C(B, T, \varepsilon)$) measurements and resistivity measurements to obtain the upper critical field $\left(B^{\rho}_{C2}(T, \varepsilon)\right)$ were performed. The basic principles of the probe design and measurement have been described in detail elsewhere [43]. A helical bending spring based on the design of Walters *et al* was used to apply strain to the sample [40]. Tensile and compressional strain was applied to the sample by twisting the spring on which the sample was mounted. The uncertainty in the strain values quoted is less than 10^{-4}.

A helical bending spring has several advantages over short-length sample measurements [16, 26, 36]. Firstly, the longer measuring length allows lower E-field sensitivity to be achieved. Indeed, recently we have reported measurements with a noise of $\sim 0.2\ \mu\mathrm{V\ m^{-1}}$ [44]. The voltage taps are well separated from the current leads, which minimizes current transfer voltages that arise from the current not fully having transferred from the matrix into the filaments [45]. A typical current transfer length for a Nb_3Sn conductor is $30d$, where d is the diameter of the conductor [46] although in short-length sample measurements first-order corrections can be made if necessary [47]. Furthermore, concerns as to whether the measurements are representative of the strand in operation, if the measurement length is less than the twist pitch (typically 10 mm) of the filaments in the strand, are avoided.

CuBe was used for the spring rather than Ti [40], Ti coated with Cu and a Ag/Cu solder [28] or brass [36]. CuBe has a high limit of elasticity, matches reasonably well the coefficient of thermal expansion of many A15 conductor composites (which often include copper for electrical and thermal stability and bronze) [43] and can be soldered directly. When the sample is soldered, it has the advantage over free-standing samples [16, 26] of allowing both tensile and compressive measurements [36, 40] as presented in this work. However, additional measurements or calculations are required to determine the strain-free state. If the sample is only soldered at the ends of the spring but not soldered in the central (voltage tap) region, measurement of the torque applied allows one to determine the properties of the strain-free state directly by measuring J_E just prior to the sample tightening significantly on the spring [48]. Although the (tensorial) strain applied is different in free-standing measurements and spring measurements, comparison of data obtained from different techniques shows that to first order the strain dependence of the critical current in the different configurations is the same [49]. Furthermore, we suggest that the spring geometry offers a more realistic configuration for the strain present in high-field magnets.

In the probe, the spring is situated in an isolated enclosure which incorporates high current lead-throughs [50] to enable variable-temperature measurements [51]. A copper gasket seal maintains the vacuum integrity of this environment and sustains the applied torque [43]. The spring design also facilitates accurate temperature control by separating the current transfer regions, where heat is generated, from the section of strand measured.

2.2.2. Improvements to the strain probe and overall accuracy. The current carrying capacity of the probe has been increased by adding more superconductor, brass and copper to the original leads. Thick brass current leads [52] were used at the top of the probe where the temperature varies from room temperature to 4.2 K. The cross-sectional area of the brass for each lead was 100 mm^2, and incorporated four 0.3 mm diameter Cu/Ni NbTi wires soldered in parallel along the entire length. The brass leads were connected to the external current terminals by eight 1 mm diameter copper wires, and at the bottom to the high-current lead-throughs (into the isolated variable-temperature enclosure) by four 1 mm diameter copper wires and four 0.36 mm diameter Cu–NbTi wires soldered in parallel. Below the lead-throughs two thicker oxygen-free high-conductivity (OFHC) copper cylindrical current leads were used in the enclosure to reduce heating around the spring. Four Ag-sheathed BiSCCO tapes were soldered in parallel on both cylindrical current leads to further reduce heating. The cylindrical current leads were connected to the spring and the high-current lead-throughs using four short lengths of 0.8 mm diameter copper wire per current lead.

To improve the temperature control during the measurements, three Cernox thermometers, which were all calibrated commercially in zero field, were mounted directly along the strand on the surface of the spring. Although these thermometers have low magnetic field dependence, there is typically an 80 mK correction at 4.2 K in magnetic fields up to 10 T [53–55]. The central control thermometer was calibrated in-house in fields up to 15 T at temperatures between 4.2 K and 20 K, as shown in figure 2 and the field-dependence accounted for in setting the temperature. The temperature along the sample was set using three independent heaters positioned concentrically about the spring. The stability of the temperature during both critical current and resistivity measurements is estimated to be <5 mK. The improved temperature control

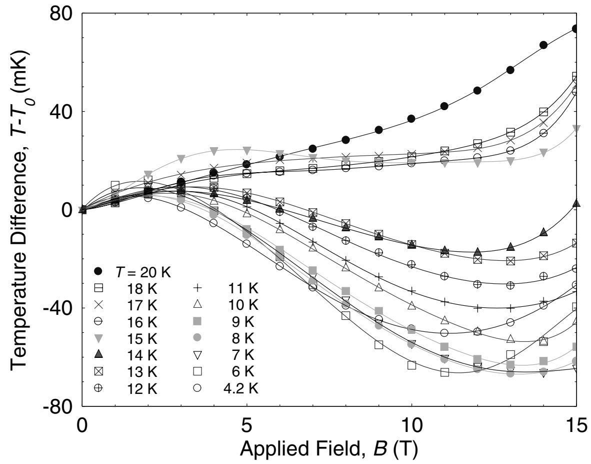

Figure 2. Temperature correction as a function of applied magnetic field for the Cernox thermometer used to control the temperature for measurements above 4.2 K. T_0 is the temperature of the thermometer in zero magnetic field. The lines are guides to the eye.

and new current leads facilitate measurements of currents up to ~200 A at 4.2 K and ~80 A at temperatures above 4.2 K, although the static boil-off of the probe has now increased by about 15%. It is estimated that the overall accuracy of the J_E data is equivalent to an uncertainty in temperature of ±100 mK. At 4.2 K, the strand is immersed directly in liquid helium with commensurately smaller overall errors.

2.2.3. Experimental method. The data acquisition followed standard procedure [45, 56]. At fixed magnetic field, temperature and strain, the current through the sample was slowly increased and the voltage across the sample monitored using a standard four-terminal V–I configuration. When the V–I transition had been recorded, I_C was extracted at a criterion of 10 μV m^{-1} or 100 μV m^{-1} and J_E calculated and stored digitally. The measurement was then repeated as a function of magnetic field. Thereafter the temperature was changed and J_E remeasured throughout the field range. The current flow direction ensured that the Lorentz force pushed the strand into the sample holder. Typical noise levels were ±1 μV m^{-1}. When the upper critical field $\left(B^{\rho}_{C2}(T, \varepsilon)\right)$ was less than 15 T, resistivity was measured as a function of field at different temperatures. A lock-in amplifier was used to provide the excitation current, at 76 Hz, and measure the generated voltage. Three different currents were used to measure the resistivity namely, 82 mA, 28 mA and 6.5 mA. The strain was then changed and J_E and resistivity measured again as a function of field and temperature. This process was repeated to obtain J_E and $B^{\rho}_{C2}(T, \varepsilon)$ in the strain range from −1.79% to +0.67%.

Critical current measurements were made in a decreasing magnetic field at 4.2 K on the first strand (Strand A) and from 6 K up to 14 K in 2 K steps on a second strand (Strand B). Resistivity measurements were made every Kelvin from 5 K to 16 K. Measurements were also made with the strand in the normal state so that the non-superconducting current flowing through the strand and the electroplated spring (i.e. the shunt) could be determined as a function of field, temperature and strain. All currents quoted in this paper have had this

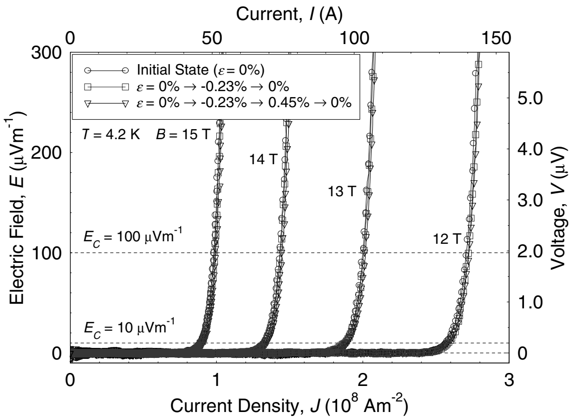

Figure 3. Electric field–current density characteristics for zero strain at 4.2 K for the Nb_3Al strand. The data demonstrate that independent of criterion, J_E is reversible. The strain was cycled as detailed in the legend.

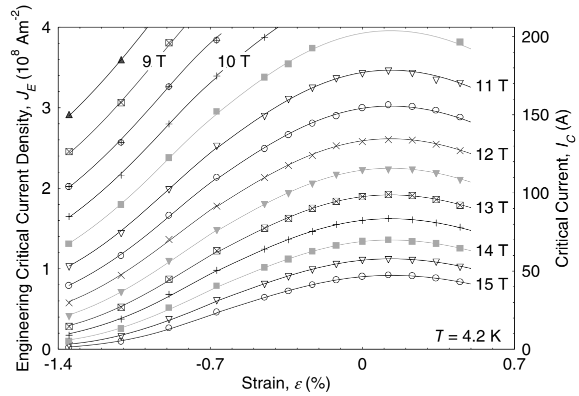

Figure 4. Engineering critical current density as a function of strain and applied magnetic field at 4.2 K for the Nb_3Al strand. The solid lines are the technological fit to the data.

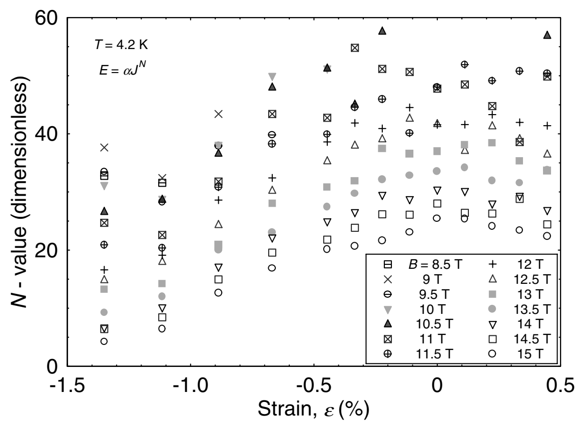

Figure 5. N-value as a function of strain and magnetic field at 4.2 K for the Nb_3Al strand. The N-value is calculated using $E = \alpha J^N$ between 10 μV m^{-1} and 100 μV m^{-1}.

current (typically 25 mA at 10 μV m^{-1}) subtracted from the total current measured in order to calculate the current in the superconductor alone [45].

3. Results

3.1. Critical current measurements

Figure 3 shows typical electric field–current density (*E–J*) characteristics as a function of applied magnetic field at 4.2 K. The data were all taken at zero strain after different strain cycles—measured before any strain was applied, after one cycle to −0.23% and after a second cycle to +0.45%. The critical current density is reversible for the different strain cycles, independent of which electric field criterion is used to define it.

In preliminary experiments, different sections of all strands that were subsequently measured in detail, were first measured at zero strain and 4.2 K to test the homogeneity of the wire. The variation in I_C of strand A, subsequently measured at 4.2 K alone, was 3.7%. The equivalent variation for strand B was 5%. To assess any possible damage that occurred during handling, a third strand was taken from the furnace and retained on the reaction mandrel for measurement. The strand was covered with a small amount of vacuum grease (which solidifies at 4.2 K). Measurements were made as a function of magnetic field at 4.2 K over several different sections of the wire. The variation in I_C in this case was 4.3%, and the magnitude of I_C was almost identical to that measured on the CuBe spring. We have concluded that within the accuracy of our measurements, there is no evidence for damage to the sample during handling.

In figure 4, J_E is shown as a function of field and strains at 4.2 K are shown. The *E*-field criterion used to define J_E over the entire data range was 10 μV m^{-1}. The solid lines are from the technological fit to the data that is described in section 4. We report that a current transfer voltage was observed at high compressive strains which only occurred when $\varepsilon < -1\%$, and was more pronounced when B_{C2} dropped below about 2 Tesla. This ohmic region in the *E–J* characteristic was below 5 μV m^{-1} at I_C. It has negligible effect on the critical current results presented in this paper, defined at 10 μV m^{-1}.

Using the standard equation, $E = \alpha J^N$, the index N has been calculated in the range from 10 μV m^{-1} to 100 μV m^{-1} and is shown in figure 5 as a function of strain at different fields at 4.2 K. Note that the symbol, *n*, is often used in the literature to denote both the index of transition of an *E–J* measurement, and the exponent of B_{C2} in the flux pinning scaling law. In order to avoid confusion, in this work, N will be used for the index of transition, and n in the flux pinning scaling law. The behaviour of J_E and N with strain at different magnetic fields is also shown at 10 K in figures 6 and 7 for comparison with the data obtained at 4.2 K. The strain at which J_E is largest (originating from the precompression exerted on the Nb_3Al filaments from copper matrix during cooling of the sample from reaction to measurement temperature [57]) is the same for both temperatures. A similar systematic dependence is noted at both temperatures for J_E and N, which is consistent with excellent temperature stability at 10 K of better than 5 mK [58]. Log–linear plots of engineering critical current density as a function of magnetic field throughout the entire temperature range at $\varepsilon = 0.45\%$ and $\varepsilon = -0.67\%$ are shown in figures 8 and 9, respectively.

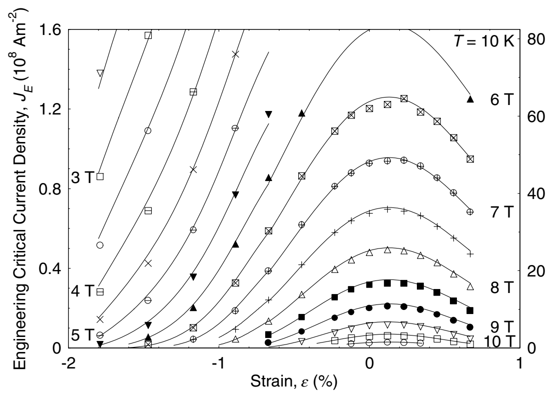

Figure 6. Engineering critical current density as a function of strain and applied magnetic field at 10 K for the Nb_3Al strand. The solid lines are the technological fit to the data.

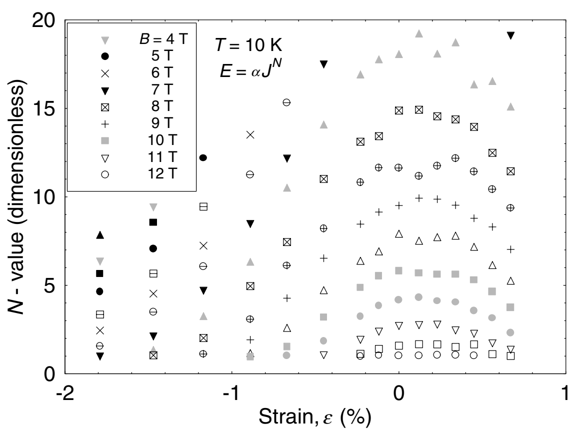

Figure 7. N-value as a function of strain and magnetic field at 10 K for the Nb_3Al strand. The N-value is calculated using $E = \alpha J^N$ between 10 μV m^{-1} and 100 μV m^{-1}.

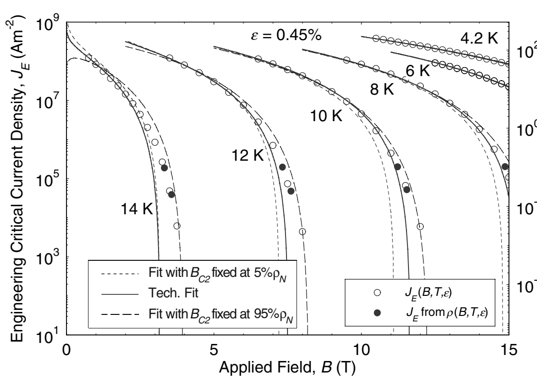

Figure 8. A log–linear plot of engineering critical current density and J_E derived from the resistivity measurement as a function of applied magnetic field and temperature at $\varepsilon = 0.45\%$ for the Nb_3Al strand. The solid line shows the technological fit to the data. The dashed lines show fits to the data constraining B_{C2} at $5\%\rho_N$ and $95\%\rho_N$.

3.2. Resistivity measurements

Typical resistivity data taken as a function of field at different temperatures and $\varepsilon = 0.45\%$ are shown in figure 10. The noise level on the measured voltage was $\sim$0.2 μV m^{-1}. The

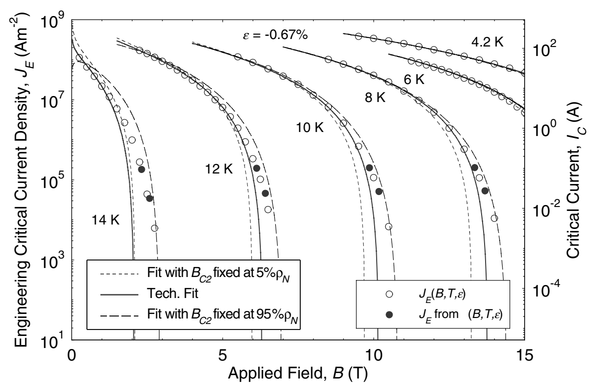

Figure 9. A log–linear plot of engineering critical current density and J_E derived from the resistivity measurement as a function of applied magnetic field and temperature at $\varepsilon = -0.67\%$ for the Nb_3Al strand. The thick solid line shows the technological fit to the data. The thin dashed lines show technological fits to the data constraining B_{C2} at $5\%\rho_N$ and $95\%\rho_N$.

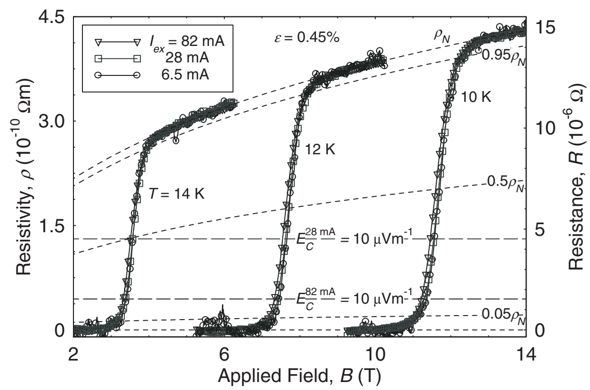

Figure 10. Resistivity as a function of magnetic field at different temperatures at $\varepsilon = 0.45\%$ for the Nb_3Al strand. The lines show the different criteria used to determine upper critical field and derive a critical current density.

resistivity data have been used to calculate I_C values close to B_{C2} as follows: when the peak ac voltage (i.e. $\sqrt{2}V_{RMS}$) generated across the sample reaches 10 μV m^{-1}, it is assumed that the peak ac current (minus the shunt current) provides the value of I_C at the applied field. It was not possible to generate I_C data for the 6.5 mA excitation because even in the normal state, the E-field generated was not sufficiently high. The construction lines to determine both B_{C2} and I_C are shown in figure 10. It should be noted that the shapes of the resistivity transition at 28 mA and 6.5 mA excitation currents are very similar. In figures 8 and 9, the inclusion of J_E obtained through the V–I and resistivity measurements demonstrates good agreement between the two types of measurement. Figure 11 shows the upper critical field determined at 50% of the normal state resistivity as a function of temperature and strain from the data obtained using 28 mA excitation current.

3.3. Comparison with other data in the literature

A comparison between data generated in Durham and that from FzK and JAERI is shown in figure 12. Figure 12(a) shows the normalized critical current as a function of strain at 4.2 K and 13 T from Durham and FzK [10]. At FzK, an axial pull rig is

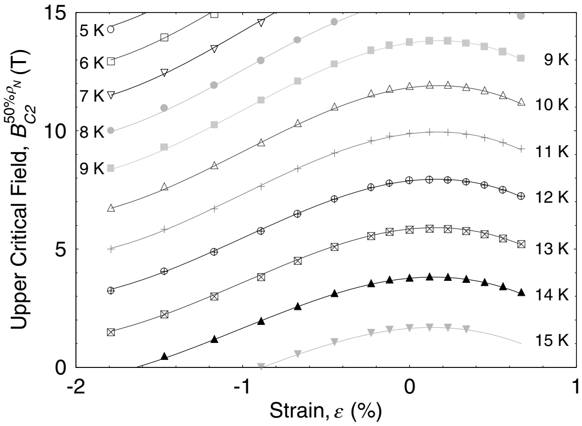

Figure 11. Upper critical field as a function of temperature and strain for the Nb_3Al strand. Upper critical field is determined at 50% of the normal state resistivity.

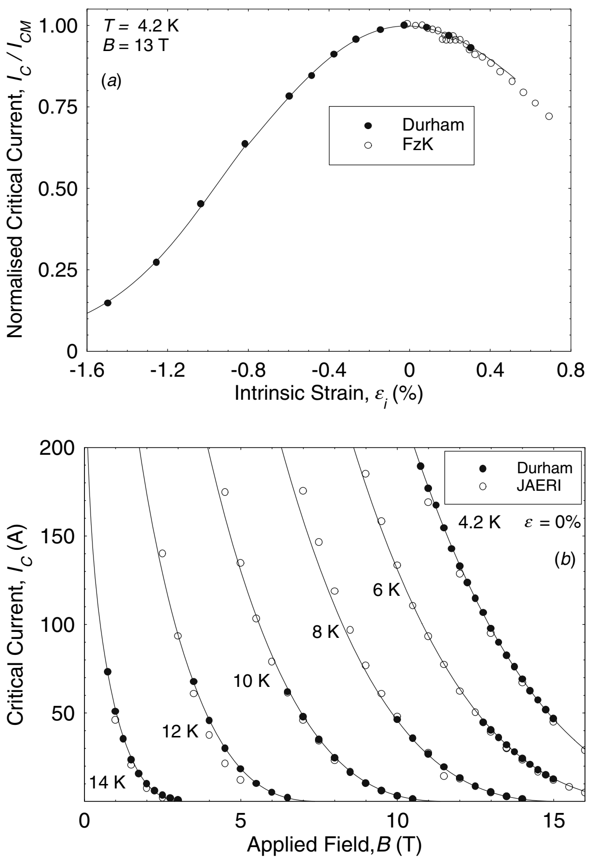

Figure 12. Comparison of critical current measurements between similar Nb_3Al strands in the literature. (*a*) Normalized critical current as a function of intrinsic strain at 13 T and 4.2 K for measurements performed in Durham and FzK [10]. (*b*) Critical current as a function of field at various temperatures and zero strain between Durham and JAERI [59]. The solid lines shown are the technological fit to the data.

used to apply strain [41]. Although the strand investigated by FzK is not identical to that studied in this paper, it is similar; so the good agreement found is expected. A similar comparison has been made between the data from Durham and FzK on

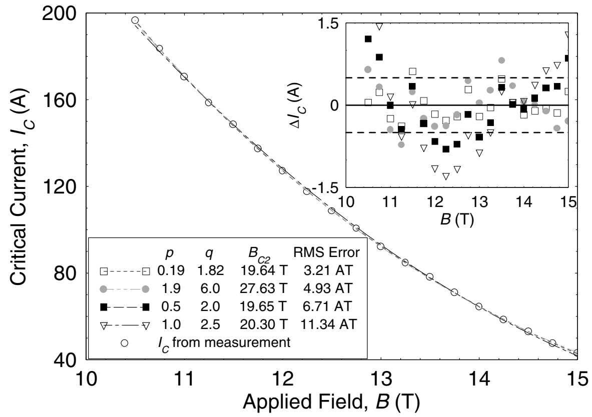

Figure 13. Critical current as a function of applied field at 4.2 K and $\varepsilon = 0.45\%$ for the Nb_3Al strand. The lines indicate four acceptable fits to the data using widely varying p and q. The errors in the legend are RMS $I_C B$ errors and the sizes of the equivalent RMS I_C errors are approximately an order of magnitude smaller (i.e. ~0.4 A and ~1 A). The inset graph shows the difference in I_C between the data and the fits.

Nb_3Sn wires and again good agreement was obtained between both the methods [49, 59]. In figure 12(*b*), comparison is made between the variable temperature data of JAERI [60] and Durham at zero strain. We conclude that there is a very good agreement between the three laboratories for I_C measured in overlapping field-temperature–strain conditions using different measurement techniques.

4. Empirical parameterization of the data

The bulk pinning force density, $F_P = J_E \times B$, for many low-temperature type-II superconductors varies with field, temperature and strain according to the semi-empirical Fietz–Webb scaling law of the form [32, 34, 61, 62]:

$$F_P = J_E \times B = C(T, \varepsilon) b^p (1 - b)^q \tag{1}$$

where b is the reduced field (B/B_{C2}) and p and q are constants. For low-temperature A15 conductors, the upper critical field data can be parameterized using the empirical equation [8, 31, 63]:

$$B_{C2}(T, \varepsilon) = B_{C2}(0, \varepsilon)\left[1 - \left(\frac{T}{T_C(\varepsilon)}\right)^{\nu}\right] \tag{2}$$

where $B_{C2}(0, \varepsilon)$ and $T_C(\varepsilon)$ are the strain-dependent upper critical field at 0 K and the critical temperature, respectively, and ν is a constant. Two alternative empirical forms for the prefactor, $C(T, \varepsilon)$, have been considered [7, 16, 26]:

$$C(T, \varepsilon) = A(T)[B_{C2}(\varepsilon)]^m \tag{3}$$

$$C(T, \varepsilon) = A(\varepsilon)[B_{C2}(T)]^n \tag{4}$$

where $A(\varepsilon$ or $T)$ is a function of strain or temperature only. The parameter m is the strain index, and n is the temperature index. These exponents have been named in this way because historically m was determined from variable-strain measurements of J_E at constant temperature and n from variable-temperature measurements of J_E at constant strain.

Figure 13 shows the critical current of the Nb_3Al strand as a function of field at 4.2 K and $\varepsilon = 0.45\%$ and scaling law fits to the data with different values of C, B_{C2}, p and q. The difference in I_C between the data and the fits is about 0.5 A (shown inset) which is within experimental error. The constants p, q and B_{C2} are strongly positively correlated. In the context of trying to distinguish which mechanism determines J_E, where change of $\frac{1}{2}$ in either p or q implies a change of mechanism (for example, surface pinning by normal precipitates leads to $p = 0.5$ and $q = 2$ whereas point pinning gives $p = 1$ and $q = 2$ [62]), the range of p and q values that are consistent with the data is enormous. Although extremely good fits can be found to parameterize the data, figure 13 demonstrates that if B_{C2} is left as a free parameter, any interpretation of a single pair of these correlated p and q values is completely unreliable.

Nevertheless, from a magnet engineering/technological perspective, the primary function of the unified scaling law is to provide an accurate mathematical description of the $J_E(B, T, \varepsilon)$ data that can be used to optimize design parameters. Whether another equivalent functional form exists is very much of a secondary interest. It is demonstrated in section 5 that a greater range of data can be more accurately parameterized using equation (4) rather than equation (3). More specifically, the errors on the temperature index, n, are lower than those for the strain index m. Combining equations (1), (2) and (4), a unified empirical relation for F_P is [8, 26]

$$F_P = J_E \times B = A^*(\varepsilon)\left\{B^*_{C2}(0,\varepsilon)\left[1-\left(\frac{T}{T^*_C}\right)^{\nu}\right]\right\}^n b^p(1-b)^q. \quad (5)$$

For simplicity, it has been assumed in the fitting procedure that the maximum in B^*_{C2}, T^*_C, J_E and the minimum in $A^*(\varepsilon)$ occur at the same strain, ε_M. The utility and accuracy of the parameterization was further improved by only considering I_C data of technological importance, namely above 1 A and by leaving B^*_{C2} as a free parameter. This latter condition improves the accuracy of the parameterization at the expense of no longer identifying B^*_{C2} with any features of the resistive transitions, or with a characteristic field of any physical significance.

In order to obtain the fitting parameters in equation (5), a preliminary global fit of all the data was made. The values of $A^*(\varepsilon)$, $T^*_C(\varepsilon)$ and $B^*_{C2}(0, \varepsilon)$ obtained in this way were then fitted to fourth-order polynomial functions where

$$\left.\begin{array}{r} A^*(\varepsilon_I) \\ B^*_{C2}(0,\varepsilon_I) \\ T^*_C(\varepsilon_I) \end{array}\right\} = c_0 + c_1\varepsilon_I + c_2\varepsilon_I^2 + c_3\varepsilon_I^3 + c_4\varepsilon_I^4 \quad (6)$$

and c_n are constants. To improve further the accuracy of the parameterization, three different ranges of temperature–strain-phase space were identified and fits to equations (5) and (6) were made in each of those ranges alone. A fit of each data set in each range was then completed with the constants in the polynomial fits and n, ν, ε_M, p and q as free parameters. The value of ε_M was found to be 0.131%. The parameterizations are described in terms of intrinsic strain ε_I, and the applied strain ε, where $\varepsilon_I = \varepsilon - \varepsilon_M$. The values found for n, p, q and ν are shown in table 1. It is understood that one can parameterize these data using a more physical form for the constants [16, 64]; however for this technological fit we have used polynomials because they provide the most accurate mathematical description of the data. The constants in the polynomial fits are shown in tables 2–4. Most of the data are parameterized to within ±1 A of the measured values. To achieve this accuracy, it is clear that a single pair of p and q values cannot be used to parameterize the entire set of data. A comparison between the measured J_E data and the technological fit is shown as a function of temperature at $\varepsilon = 0.45\%$ and $\varepsilon = -0.67\%$ in figures 8 and 9, respectively. The fit only starts to break down at very high temperatures and high compressive strains where B^*_{C2} is of the order of 2 T. Also shown in figures 8 and 9 are fits to the data where B_{C2} has been constrained at $5\%\rho_N$ and $95\%\rho_N$, and p, q, n, and ν are assumed single-valued throughout the entire range of data. It can be seen that the fits constrained at $95\%\rho_N$ fit the high field, low J_E tail well, but do not provide a good overall fit. On the other hand, defining B_{C2} at $5\%\rho_N$ provides a better overall fit to the data at the expense of not fitting the low J_E data.

Table 1. Constants derived from the technological fit to the critical current data for the Nb_3Al strand.

Data range	p	q	n	ν
$4.2\ K \leqslant T \leqslant 10\ K$, $-0.67\% \leqslant \varepsilon \leqslant 0.67\%$	0.845	2.740	2.301	1.323
$4.2\ K \leqslant T \leqslant 10\ K$, $-1.79\% \leqslant \varepsilon < -0.67\%$	1.125	2.893	2.392	1.250
$10\ K < T \leqslant 14\ K$, $-1.79\% \leqslant \varepsilon \leqslant 0.67\%$	0.787	2.756	2.249	1.403

The upper critical field that was determined from the resistivity data defined at 5%, 50% and 95% of the normal state resistivity has been parameterized using equation (2). Values for ν are presented in table 5, along with the standard deviation of the fit to each data set. $B^{\rho_N}_{C2}(0, \varepsilon)$ and $T^{\rho_N}_C(\varepsilon)$ defined at 5%, 50% and 95% of the normal state resistivity have been also parameterized using fourth-order polynomial fits and the constants given in table 6. Figure 14 shows the scaling of the upper critical field defined at a criterion of $50\%\rho_N$. Good scaling of the data was also observed for $B^{\rho_N}_{C2}(T, \varepsilon)$ defined at $5\%\rho_N$ and $95\%\rho_N$. In figures 15 and 16, $T^{\rho_N}_C(\varepsilon)$ and $B^{\rho_N}_{C2}(0, \varepsilon)$ are plotted as a function of strain. Note that for these optimized empirical fits to the data, the strains at which $T^{\rho_N}_C(\varepsilon)$ and $B^{\rho_N}_{C2}(0, \varepsilon)$ are maximum are found to be $\varepsilon_M = 0.13\%$ and $\varepsilon_M = 0.20\%$, respectively. Also shown are the effective $T^*_C(\varepsilon)$ and $B^*_{C2}(0, \varepsilon)$ that are derived from the technological fit. Figures 15 and 16 allow comparison between $B^{\rho_N}_{C2}(0, \varepsilon)$ and $T^{\rho_N}_C(\varepsilon)$ extracted from the parameterization of the upper critical field data from the resistivity measurements and the technological fit to the critical current data. There is no simple relation between B_{C2} derived from these different measurements. The data from the resistivity measurements in figures 15 and 16 have been replotted in figure 17. The linearity and double-valued behaviour has also been observed in Nb_3Sn (derived from extrapolating J_E values to zero) [8, 65]. In both materials, the linearity had a positive gradient and negative intercept on the $B^{\rho_N}_{C2}(0, \varepsilon)$ axis.

5. A single scaling law

To proceed beyond the empirical scaling laws, we need to break the strong correlation between p, q and B_{C2}. This can be done, in principle, by measuring B_{C2} resistively. However, technological conductors are not homogeneous. Inevitably, the field at which the critical current density drops to zero represents the upper critical field for the percolative path

Table 2. Free parameters for the technical parameterization in the range $-0.67\% \leqslant \varepsilon \leqslant +0.67\%$, $4.2\ \mathrm{K} \leqslant T \leqslant 10\ \mathrm{K}$ for the Nb_3Al strand.

$-0.67\% \leqslant \varepsilon \leqslant +0.67\%$, $4.2\ \mathrm{K} \leqslant T \leqslant 10\ \mathrm{K}$	$A^*(\varepsilon)(\mathrm{A}^{-2}\ \mathrm{T}^{-2.301})$	$B^*_{C2}(0,\varepsilon)$ (T)	$T^*_C(\varepsilon)$ (K)
c_0	3.942×10^7	26.26	15.81
c_1	0	0	0
c_2	5.424×10^{10}	-3.264×10^4	-1.255×10^4
c_3	-3.096×10^{12}	6.521×10^5	2.202×10^5
c_4	-3.608×10^{14}	1.156×10^8	4.190×10^7

Table 3. Free parameters for the technical parameterization in the range $-1.79\% \leqslant \varepsilon < -0.67\%$, $4.2\ \mathrm{K} \leqslant T \leqslant 10\ \mathrm{K}$ for the Nb_3Al strand.

$-1.79\% \leqslant \varepsilon < -0.67\%$, $4.2\ \mathrm{K} \leqslant T \leqslant 10\ \mathrm{K}$	$A^*(\varepsilon)$ $(\mathrm{A}^{-2}\ \mathrm{T}^{-2.392})$	$B^*_{C2}(0,\varepsilon)$ (T)	$T^*_C(\varepsilon)$ (K)
c_0	2.552×10^7	23.18	12.52
c_1	-3.567×10^9	-1.535×10^3	-1.126×10^3
c_2	-2.028×10^{11}	-2.617×10^5	-1.459×10^5
c_3	-6.839×10^{12}	-1.382×10^7	-7.206×10^6
c_4	-1.250×10^{14}	-2.524×10^8	-1.307×10^8

Table 4. Free parameters for the technical parameterization in the range $-1.79\% \leqslant \varepsilon \leqslant +0.67\%$, $10\ \mathrm{K} < T \leqslant 14\ \mathrm{K}$ for the Nb_3Al strand.

$-1.79\% \leqslant \varepsilon \leqslant +0.67\%$, $10\ \mathrm{K} < T \leqslant 14\ \mathrm{K}$	$A^*(\varepsilon)$ $(\mathrm{A}^{-2}\ \mathrm{T}^{-2.249})$	$B^*_{C2}(0,\varepsilon)$ (T)	$T^*_C(\varepsilon)$ (K)
c_0	4.455×10^7	25.88	15.49
c_1	0	0	0
c_2	4.416×10^{10}	-3.024×10^4	-1.017×10^4
c_3	3.244×10^{12}	5.446×10^5	-1.737×10^5
c_4	7.452×10^{13}	6.801×10^7	5.646×10^5

Table 5. Upper critical field scaling law parameter (ν) derived from the resistivity data and the standard deviation on the fit to the data for the Nb_3Al strand.

Upper critical field defined at	ν (dimensionless)	Standard deviation (mT)
$5\%\rho_N$	1.25	38.9
$50\%\rho_N$	1.27	33.5
$95\%\rho_N$	1.31	30.2

Table 6. Free parameters for the technical parameterization of the upper critical field data for the Nb_3Al strand.

$T^\rho_C(\varepsilon)$ (K) defined at	$5\%\rho_N$	$50\%\rho_N$	$95\%\rho_N$
c_0	15.63	15.78	15.91
c_1	0	0	0
c_2	-1.040×10^4	-9.736×10^3	-9.853×10^3
c_3	-9.337×10^4	-1.832×10^5	-1.769×10^5
c_4	7.034×10^6	2.622×10^6	3.564×10^6
$B^\rho_{C2}(0,\varepsilon)$ (T) defined at	$5\%\rho_N$	$50\%\rho_N$	$95\%\rho_N$
c_0	26.53	27.08	27.48
c_1	0	0	0
c_2	-3.529×10^4	-3.908×10^4	-3.755×10^4
c_3	-4.971×10^5	-8.122×10^5	-7.018×10^5
c_4	1.876×10^7	1.192×10^7	1.364×10^7

through the material with the highest B_{C2}. This high B_{C2} value is not representative of the material. Physical interpretation of the J_E data is required to eliminate non-physical solutions, identify a characteristic value of B_{C2} (where the critical current may not be zero) and hence identify a scaling law that can be used to address the science that underlies the mechanism that determines the critical current density.

In figure 18, RMS $I_C B$ error surfaces are shown for p and q derived from the variable magnetic field data at 4.2 K for (*a*) $\varepsilon = 0.45\%$, at 8 K for (*b*) $\varepsilon = -1.79\%$ and at 10 K for (*c*) $\varepsilon = 0.45\%$ and (*d*) $\varepsilon = -1.79\%$. The ranges of the fields over which these data were taken were (a) 10.5–15 T, (b) 8.5–15 T, (c) 6–11.5 T, (d) 2.5–7 T, respectively. The solid contours are logarithmically separated for each decade as indicated in the legend and the dashed contour shows the approximate maximum RMS $I_C B$ error that still provides an acceptable fit. From the fit to the data, B_{C2} and C values are also generated. The figure shows solid curves giving p–q pair-values when B_{C2} takes the value determined from the resistivity measurements at $5\%\rho_N$, $50\%\rho_N$ and $95\%\rho_N$. The upper critical field values at 4.2 K are extrapolated values from the parameterization detailed above (see equation (2)). Across the entire data set, a large shallow minimum in the error surface is found, leading to a wide range of p and q values consistent with the results shown in figure 13. The area of this shallow region is larger at 4.2 K and 6 K where it is not possible to measure close to B_{C2}. At higher temperatures, where measurement of B_{C2} is possible, the minimum in the error surface tends to coincide with the upper critical field defined at $95\%\rho_N$, but the allowed range of p and q values is still very large.

The data from 8 K to 14 K, where the upper critical field was directly measured, were then refitted with p, q and C left unconstrained and B_{C2} constrained to the value at $5\%\rho_N$, $50\%\rho_N$ or $95\%\rho_N$. The values of p and q obtained are shown in figures 19 and 20, respectively, with averages denoted by the horizontal lines at each temperature. The data constrained

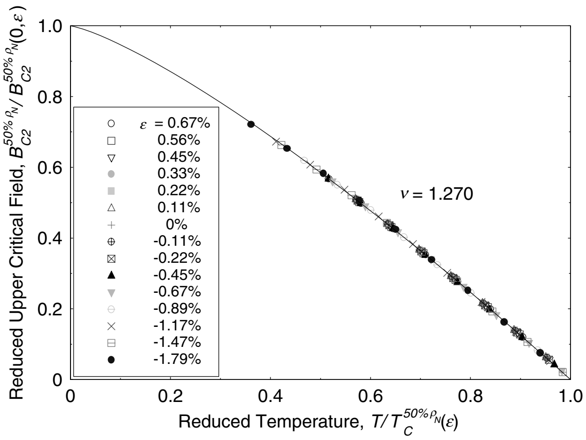

Figure 14. A universal scaling law showing the reduced upper critical field as a function of reduced temperature at different applied strains for the Nb_3Al strand.

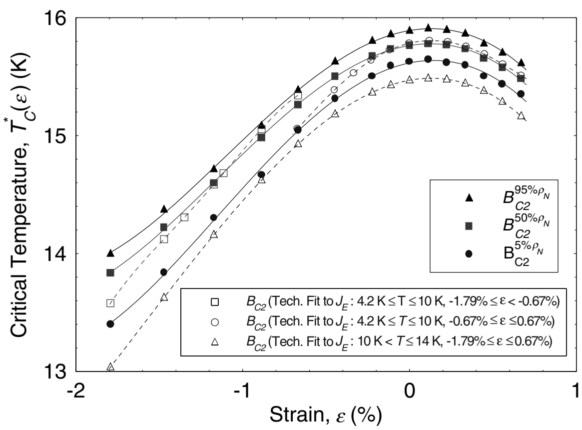

Figure 15. Effective critical temperature as a function of applied strain for the Nb_3Al strand. The solid symbols represent data obtained from the ac resistivity measurement of B_{C2}. The open symbols are derived from the technological fit to the critical current data. The lines are fourth-order polynomial fits that parameterize the data.

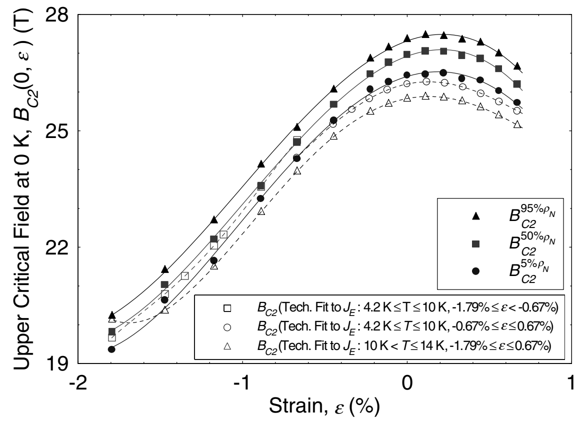

Figure 16. Effective upper critical field at 0 K as a function of applied strain for the Nb_3Al strand. The solid symbols represent data obtained from the ac resistivity measurement of B_{C2}. The open symbols are derived from the technological fit to the critical current data. The lines are fourth-order polynomial fits that parameterize the data.

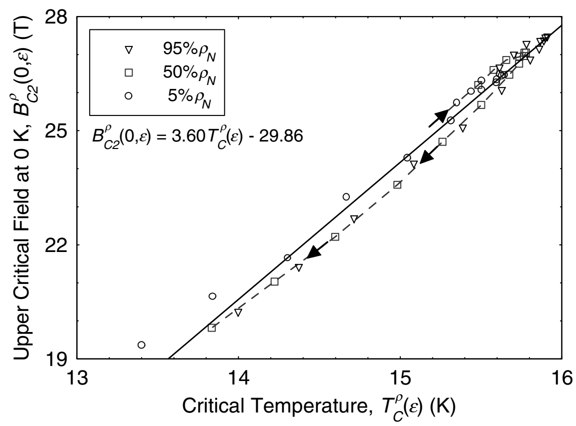

Figure 17. Effective upper critical field at 0 K as a function of the effective critical temperature for the Nb_3Al strand. The internal variable is the applied strain. The dashed line indicates the double-valued behaviour in the data with the arrows indicating decreasing strain.

at $5\%\rho_N$ are single valued—independent of temperature and strain within the errors of the measurement. The average values of p and q are $p = 0.39 \pm 0.19$ and $q = 2.16 \pm 0.10$. For B_{C2} constrained at $50\%\rho_N$ and $95\%\rho_N$, p and q are both strong functions of temperature and q is also a function of strain. The average values of p and q obtained for B_{C2} constrained at $5\%\rho_N$, $50\%\rho_N$ or $95\%\rho_N$ at each temperature are shown in table 7. We conclude that the value of B_{C2} determined at $5\%\rho_N$ is required for p and q to be constant and hence for F_P to scale accurately.

Since the values of p and q that produce good scaling are close to the Kramer values [34] of $p = 0.5$ and $q = 2$ that are very widely used [27, 28, 35, 37–39, 66, 67], this paper also considers the implications of making the assumption that they are valid. The J_E data presented in figures 8 and 9 have been replotted on a Kramer plot in figures 21 and 22. The straight line fits to the Kramer plots have been generated by ignoring the I_C data below 5 A (9.7×10^6 A m^{-2}). Also shown are the values for B_{C2} obtained from the resistivity measurements. The extrapolated Kramer B_{C2} value is typically 300 mT less than that defined at $5\%\rho_N$.

Using $p = 0.39$, $q = 2.16$ and constraining $B_{C2}^{\rho_N}(T,\varepsilon)$ at $5\%\rho_N$, the form of the prefactor can be determined from log–log plots of C as a function of $B_{C2}^{\rho_N}$. Figure 23 plots $C(\varepsilon)$ as a function of $B_{C2}^{\rho_N}(\varepsilon)$ at constant temperatures to give m. The data have been normalized for clarity and show in detail the technologically important region from about $-0.5\% \leqslant \varepsilon \leqslant 0.67\%$. The inset graph shows the entire data set. Figure 24 provides $C(T)$ as a function of $B_{C2}^{5\%\rho_N}(T)$ at constant strain which gives n. Here each data set is offset from the previous one by $\log_{10}(C) = -0.2$. In both figures, at high compressive strains and at 14 K linearity breaks down. It can be seen that m and n are almost independent of temperature. In the ranges $-0.5\% \leqslant \varepsilon \leqslant 0.67\%$ and $8\ \text{K} \leqslant T \leqslant 12$ K, $m = 1.87 \pm 0.08$ and $n = 2.18 \pm 0.02$. The associated parameters $A(\varepsilon)$ and $A(T)$ are presented in figure 25. The error in m is a factor 4 higher than n. This primarily occurs because at constant strain (when varying temperature) the prefactor C is a unique

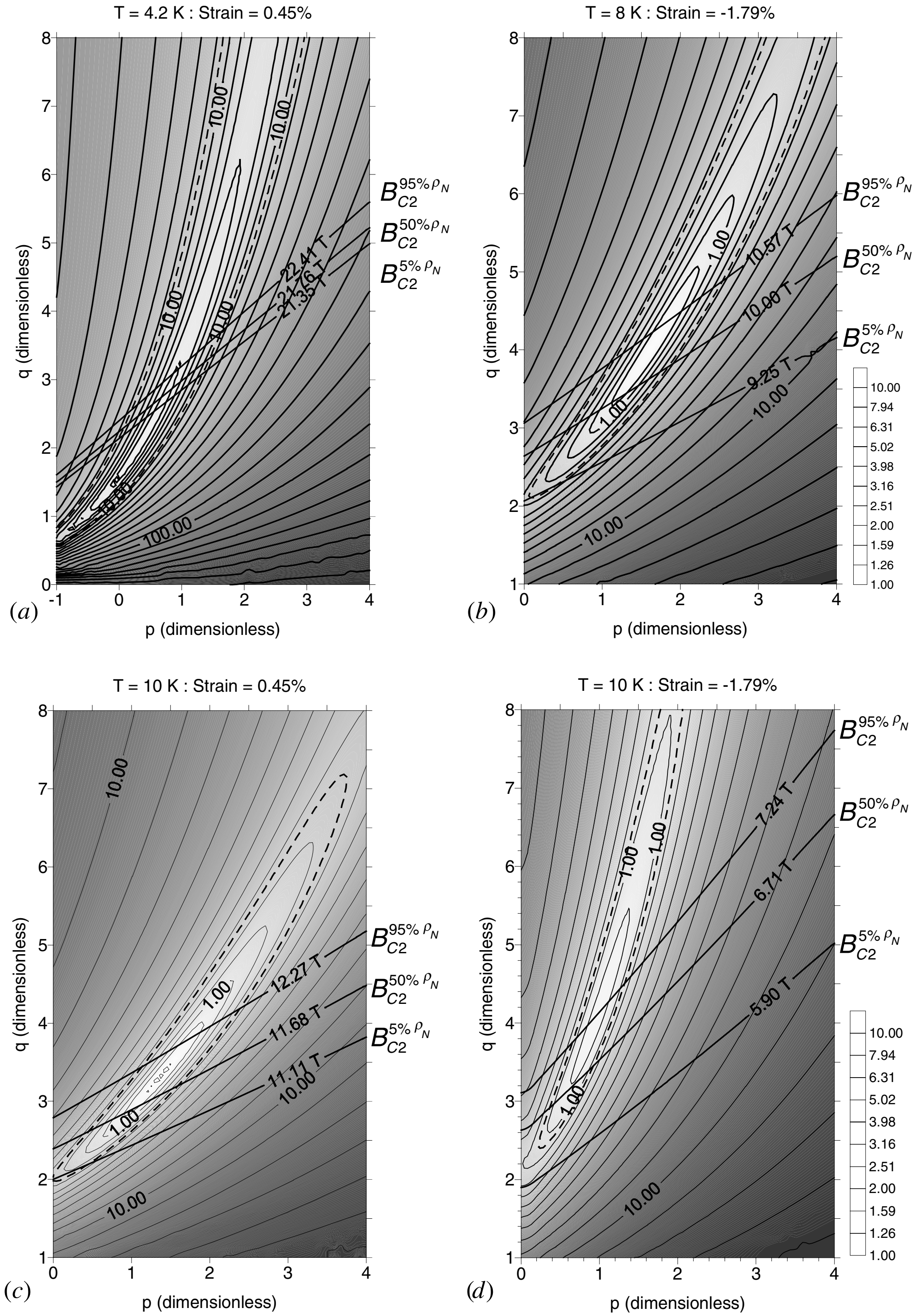

Figure 18. RMS $I_C B$ error surface plots as a function of p and q from fitting to the data at (a) 4.2 K and $\varepsilon = 0.45\%$, (b) 8 K and $\varepsilon = -1.79\%$, (c) 10 K and $\varepsilon = 0.45\%$ and (d) 10 K and $\varepsilon = -1.79\%$ for the Nb_3Al strand. The dashed line indicates the maximum RMS error for an acceptable fit. The solid curves give p, q pair-values when the upper critical field is constrained by B_{C2} from the resistivity data. The contours on the error surface are logarithmically spaced per decade as indicated in the legend.

function of B_{C2}, whereas C is a double-valued function of B_{C2} (with varying strain) at constant temperature as shown by the arrows in figure 23 and also found in Nb_3Sn [65]. Hence, the parameterization of the prefactor C is most accurately achieved in the form of equation (4) as found for Nb_3Sn [7, 8]. Note that when p and q are fixed, C is proportional to the maximum

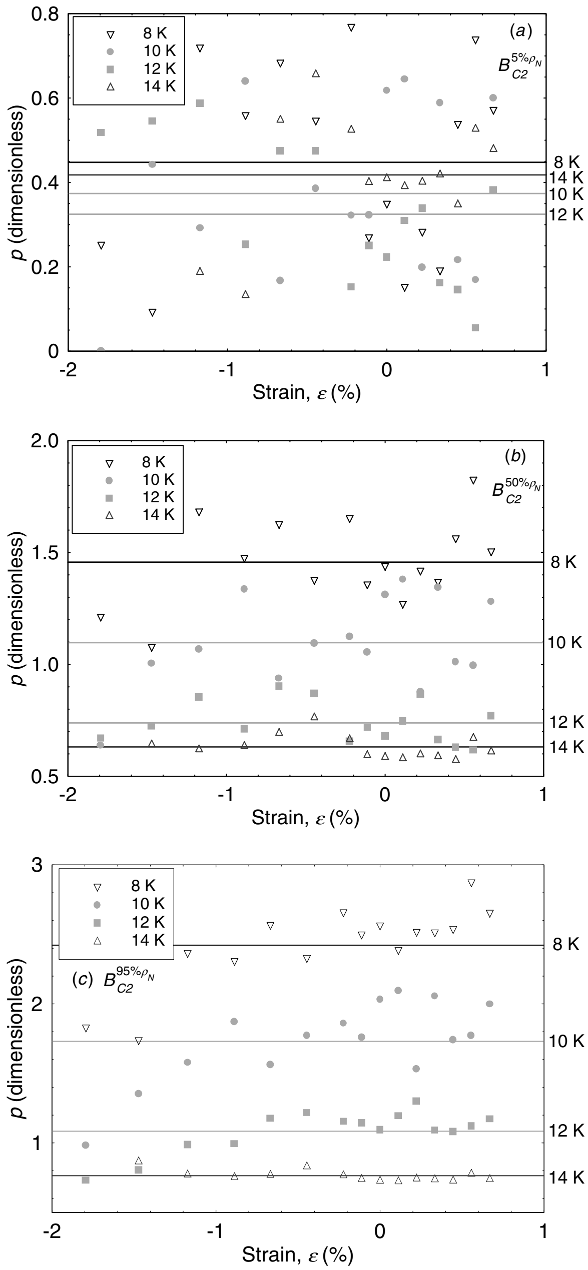

Figure 19. Scaling law exponent, p, as a function of strain for the Nb_3Al strand. The data were obtained from a fit constraining B_{C2} at (*a*) $5\%\rho_N$, (*b*) $50\%\rho_N$ and (*c*) $95\%\rho_N$. The solid lines show average values for the data in the range $-1.79\% \leqslant \varepsilon \leqslant 0.67\%$.

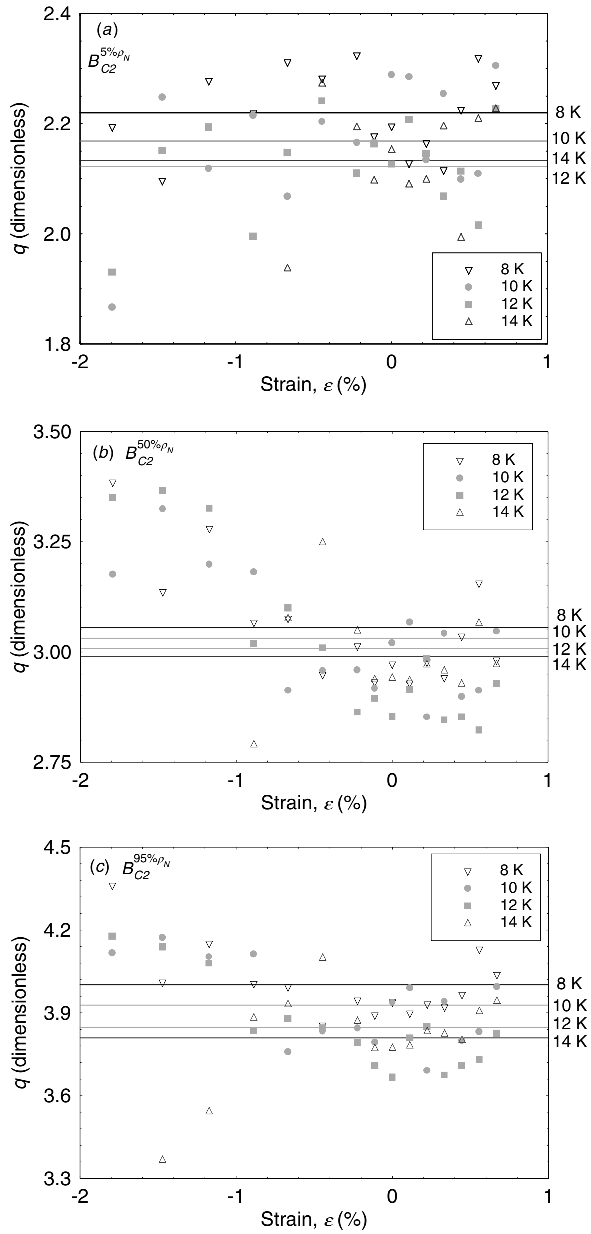

Figure 20. Scaling law exponent, q, as a function of strain for the Nb_3Al strand. The data were obtained from a fit constraining B_{C2} at (*a*) $5\%\rho_N$, (*b*) $50\%\rho_N$ and (*c*) $95\%\rho_N$. The solid lines show average values for the data in the range $-1.79\% \leqslant \varepsilon \leqslant 0.67\%$.

value of F_P found when varying magnetic field. In figure 26, a log–log plot of $C(T, \varepsilon)$ as a function of $B_{C2}(T, \varepsilon)$ is presented. The values of B_{C2} at 4.2 K and 6 K are extrapolated values derived from the parameterization using equation (2). Equivalent data derived from the Kramer plots are also shown in figure 26 (offset by $\log_{10}(C) = -1$). This analysis therefore leads to a scaling law given by

$$F_P = A(\varepsilon)\left[B_{C2}^{5\%\rho_N}(T, \varepsilon)\right]^{2.18} b^{0.39}(1 - b)^{2.16} \tag{7}$$

or for the Kramer parameterization $n = 2.30 \pm 0.14$.

Although one can parameterize C using equation (7) or an equivalent Kramer form, it is clear that any complete description of F_P must include the Ginzburg–Landau parameter, $\kappa(T, \varepsilon)$. Unfortunately κ is not measured in transport measurements directly. Nevertheless we now consider how to incorporate κ into the scaling law. Using the equation for the thermodynamic critical field at zero temperature $B_C(0, \varepsilon) = 7.65 \times 10^{-4} \gamma^{\frac{1}{2}} T_C(\varepsilon)$ [68] with the two-fluid model for the temperature dependence $B_C(T, \varepsilon) = B_C(0, \varepsilon)[1 - t^2]$ and the Ginzburg–Landau relation for the

Table 7. Average values of p and q as a function of temperature for the Nb_3Al strand from the fits to the data in the strain range $-1.79\% \leqslant \varepsilon \leqslant 0.67\%$ where B_{C2} is constrained by resistivity measurement.

	B_{C2} defined at $5\%\rho_N$		B_{C2} defined at $50\%\rho_N$		B_{C2} defined at $95\%\rho_N$	
T (K)	p	q	p	q	p	q
8	0.45 ± 0.23	2.22 ± 0.08	1.46 ± 0.19	3.06 ± 0.13	2.42 ± 0.30	4.00 ± 0.13
10	0.37 ± 0.21	2.17 ± 0.11	1.10 ± 0.21	3.03 ± 0.14	1.73 ± 0.30	3.93 ± 0.15
12	0.32 ± 0.17	2.12 ± 0.09	0.74 ± 0.09	3.01 ± 0.19	1.08 ± 0.15	3.85 ± 0.16
14	0.42 ± 0.14	2.13 ± 0.10	0.63 ± 0.05	2.99 ± 0.11	0.76 ± 0.04	3.81 ± 0.18
Global fit	0.39 ± 0.19	2.16 ± 0.10	n/a	n/a	n/a	n/a

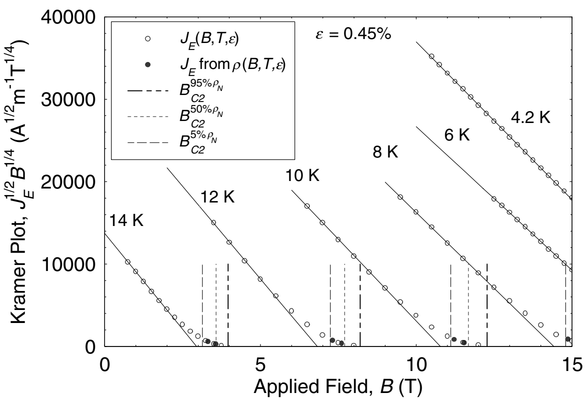

Figure 21. Kramer plot as a function of temperature at $\varepsilon = 0.45\%$ for the Nb_3Al strand. The solid lines are fits to the data using a Kramer analysis. The dashed lines indicate the upper critical field defined at $5\%\rho_N$, $50\%\rho_N$ and $95\%\rho_N$.

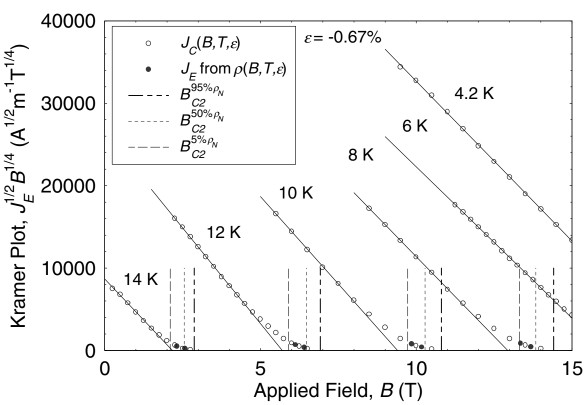

Figure 22. Kramer plot as a function of temperature at $\varepsilon = -0.67\%$ for the Nb_3Al strand. The solid lines are fits to the data using a Kramer analysis of the data. The dashed lines indicate the upper critical field defined at $5\%\rho_N$, $50\%\rho_N$ and $95\%\rho_N$.

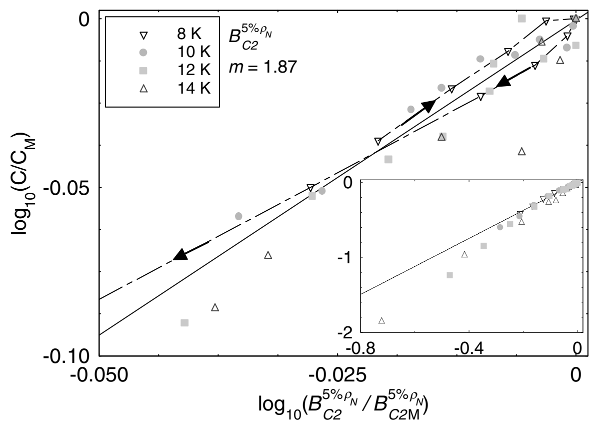

Figure 23. Normalized log–log plot of the scaling law prefactor, C, against upper critical field as a function of strain at constant temperature for the Nb_3Al strand. The data were obtained from a fit constraining B_{C2} at $5\%\rho_N$. C_M and B_{C2M} are the maximum values for the prefactor and upper critical field, respectively. The main graph shows data typically in the strain range $0.5 \leqslant \varepsilon \leqslant 0.67\%$ and the inset shows the entire data set. The solid line gives a global average for m. The dashed line indicates the hysteresis on the 8 K data. The arrows indicate decreasing strain.

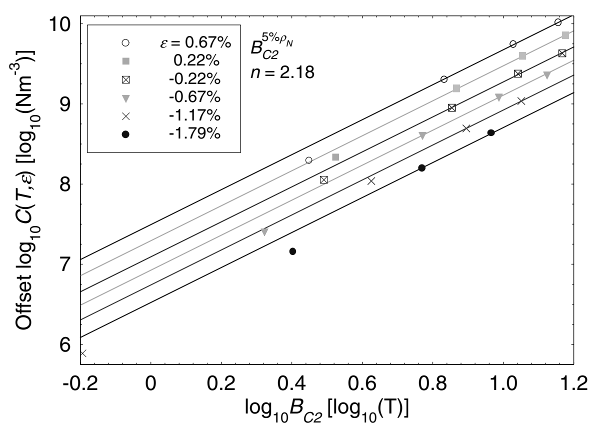

Figure 24. Offset log–log plot of the scaling law prefactor, C, against upper critical field as a function of temperature at constant strain for the Nb_3Al strand. The data were obtained from a fit constraining B_{C2} at $5\%\rho_N$. Each curve is offset from the one above by 0.2. The solid lines give a global average for n.

upper critical field $B_{C2}(T, \varepsilon) = \sqrt{2}\kappa(T, \varepsilon)B_C(T, \varepsilon)$, an empirical relation for κ has been found of the form [35, 69]

$$\kappa(T, \varepsilon) = \frac{B_{C2}(T, \varepsilon)}{\sqrt{2}B_C(T, \varepsilon)} = 924\frac{B_{C2}(T, \varepsilon)}{\gamma^{\frac{1}{2}}(\varepsilon)T_C(\varepsilon)[1 - t^2]} \tag{8}$$

where $t = T/T_C(\varepsilon)$ and γ is the Sommerfeld constant. In figure 27, $\kappa\gamma^{1/2}$ is plotted as a function of strain. $T_C(\varepsilon)$ has been calculated from the fit to the $B_{C2}^{5\%\rho_N}(T, \varepsilon)$ data using equation (2). There is a systematic dependence for $\gamma^{1/2}\kappa$ in the data as a function of strain and temperature except close to T_C. Equation (8) can be rewritten using equation (2) and L'Hospital's rule [70] to provide a form useful for considering the temperature dependence for κ of the form

$$\frac{\kappa(T, \varepsilon)}{\kappa(T_C, \varepsilon)} = \frac{2}{\nu}\frac{[1 - t^\nu]}{[1 - t^2]}. \tag{9}$$

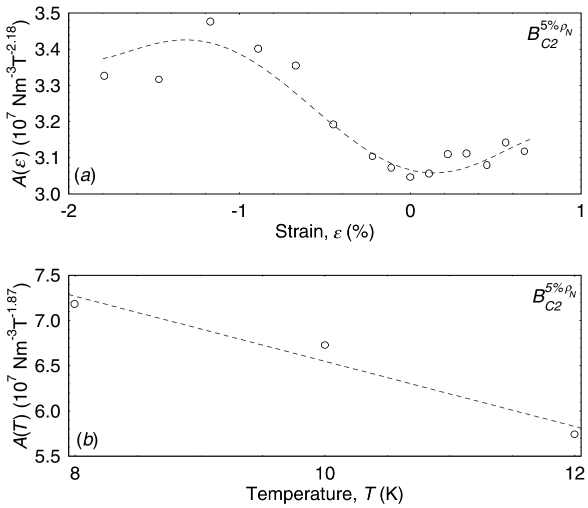

Figure 25. Prefactor (*a*) $A(\varepsilon)$ as a function of strain and (*b*) $A(T)$ as a function of temperature from fits constraining upper critical field at $5\%\rho_N$ for the Nb_3Al strand. The dashed lines are guides to the eye.

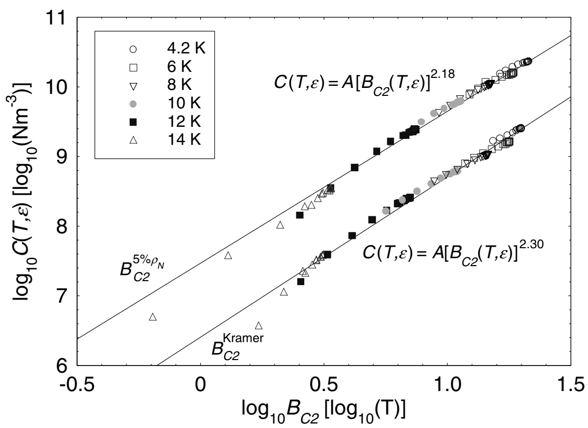

Figure 26. Log–log plot of the scaling law prefactor, C, against upper critical field as a function of strain at constant temperature generated using B_{C2} constrained at $5\%\rho_N$ and from a Kramer analysis of the data for the Nb_3Al strand. The solid lines are defined by the equations in the figure. The data from the Kramer analysis have been offset by $\log C = -1$.

To evaluate $\kappa(T_C, \varepsilon)$, equation (8) can also be rewritten using L'Hospital's rule to give

$$\kappa(T_C, \varepsilon) = 924 \frac{B_{C2}(0, \varepsilon)}{\gamma^{\frac{1}{2}}(\varepsilon) T_C(\varepsilon)} \frac{\nu}{2}. \tag{10}$$

Using the strain dependence of $B_{C2}(0, \varepsilon)$ and $T_C(\varepsilon)$ given in table 6, and the value for ν in table 5, the resulting dependence of $\gamma^{\frac{1}{2}}(\varepsilon)\kappa(T_C, \varepsilon)$ can be found. This has been plotted in figure 27 as a solid line. In order to calculate a value of κ, γ is required. Measurements on bulk Nb_3Al [71, 72] and thin films with varying stoichiometry [73] give a typical value for the Sommerfeld coefficient for the electronic specific heat in Nb_3Al of 720 ± 50 J K^{-2} m^{-3}. This leads to value for $\kappa(T_C, \varepsilon = 0)$ calculated to be 36.5 ± 1.3 which can be compared to a value of $\sim$33 for Nb_3Sn [74]. The data in figure 27 have been normalized at T_C and replotted in figure 28. Figure 28 includes normalized kappa values derived using B_{C2} from the Kramer plots for the Nb_3Al strand; values derived from the literature for $(NbTa)_3Sn$ [35], and NbTi [75]; solid lines showing equation (9) for different values of ν; and a dashed line giving experimental data for Nb from the literature [76]. The different A15 compounds show similar temperature dependencies. In figure 29, $C\kappa^2\gamma$ is plotted as a function of the upper critical field and temperature at different strains on a log–log plot. The data at each strain were individually fitted using a linear function. The gradient was found to be $n = 2.60 \pm 0.06$ with an intercept of $C\kappa^2\gamma = (1.44 \pm 0.25) \times 10^{13}$ J^2 K^{-2} m^{-7}. The equivalent data using the Kramer analysis have also been plotted in figure 29, but offset by $\log_{10}(C\kappa^2\gamma) = -1$. This procedure was repeated for the Kramer analysis resulting in $n = 2.53 \pm 0.12$ and an intercept of $C\kappa^2\gamma = (1.62 \pm 0.70) \times 10^{13}$ J^2 K^{-2} m^{-7}. The linearity of the data in figure 29 implies

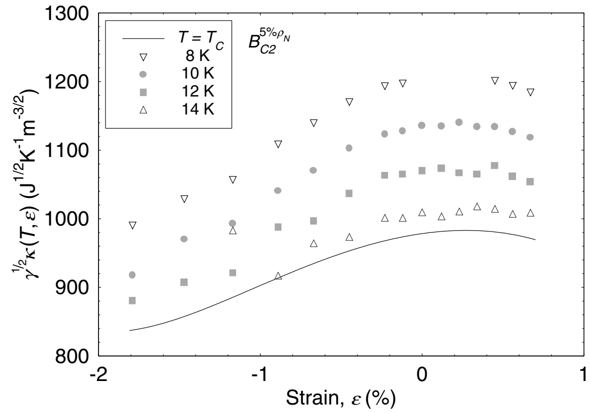

Figure 27. The parameter $\gamma^{1/2}\kappa$ as a function of strain and temperature for the Nb_3Al strand when B_{C2} is defined at $5\%\rho_N$. The Ginzburg–Landau parameter is κ and γ is the Sommerfeld constant for the electronic specific heat. The solid line plots the calculated value of $\gamma^{1/2}\kappa$ at $T = T_C$.

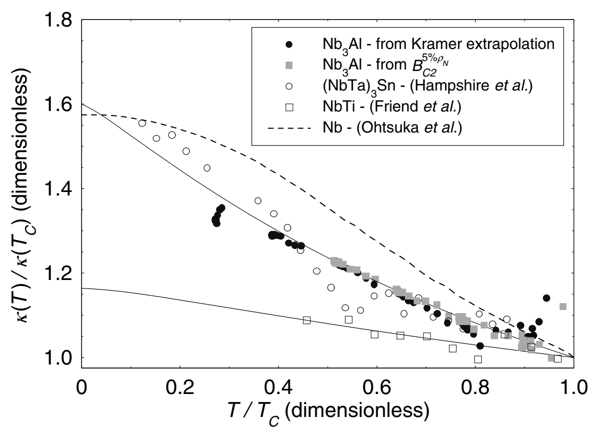

Figure 28. Normalized κ as a function of reduced temperature for the Nb_3Al strand, a commercial NbTi strand (taken from resistivity data) [74], a commercial $(NbTa)_3Sn$ strand (taken from a Kramer extrapolation to J_C data) [34] and a high purity Nb sample (from magnetocaloric data) [75]. The upper and lower solid lines are calculated using $\nu = 1.25$ and $\nu = 1.72$ respectively.

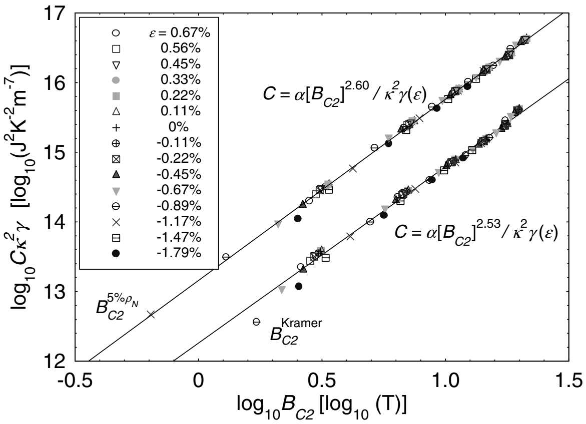

Figure 29. Log–log plot of $C\kappa^2\gamma$ as a function of upper critical field and temperature at different strains generated using B_{C2} constrained at $5\%\rho_N$ and from a Kramer analysis of the data for the Nb_3Al strand. The solid lines are lines of best fit to the entire data sets. The data from the Kramer analysis have been offset by $\log C\kappa^2\gamma = -1$.

that to a good approximation

$$C(T, \varepsilon) = G(\varepsilon)\frac{\left[B_{C2}^{5\%\rho_N}(T, \varepsilon)\right]^{2.60}}{\kappa^2(T, \varepsilon)\gamma(\varepsilon)}. \quad (11)$$

Hence the temperature dependence of $C(T, \varepsilon)$ is accurately characterized by the factor $\frac{\left[B_{C2}^{5\%\rho_N}(T,\varepsilon)\right]^{2.60}}{\kappa^2(T,\varepsilon)}$. There is no need for any additional temperature-dependent terms. Uncertainty in the intercept values in figure 29 gives an uncertainty in $G(\varepsilon)$ of about 15%. $G(\varepsilon)$, n and $T_C(\varepsilon)$ are tabulated as a function of strain in table 8 for the analysis where B_{C2} is defined at $5\%\rho_N$ using $p = 0.39$ and $q = 2.16$ and the Kramer analysis using $p = 0.5$ and $q = 2$. $G(\varepsilon)$ is very broadly consistent with an inverse parabola with a value about 40% lower at strong compression than its peak value at 0.11% strain. To the author's knowledge, the uniaxial strain dependence of the Sommerfeld constant (or density of states at the Fermi surface) in Nb_3Al has not been reported. However, hydrostatic measurements on Nb_3Sn [77] show that a change in T_C of ~0.35 K produces a change in $\gamma(\varepsilon)$ of ~8%. In the strain measurements presented here on Nb_3Al, T_C changed by about 2 K, so we tentatively attribute the 40% change in $G(\varepsilon)$ to the strain dependence of $\gamma(\varepsilon)$. Hence assuming $\gamma(\varepsilon = 0) = 720$ J K^{-2} m^{-3}, equation (7) becomes

$$F_P = \frac{1}{337}\frac{\left[B_{C2}^{5\%\rho_N}(T, \varepsilon)\right]^{2.60}}{(2\pi\Phi_0)^{\frac{1}{2}}\mu_0\kappa^2(T, \varepsilon)}b^{0.39}(1-b)^{2.16} \quad (12)$$

or for the Kramer analysis in which I_C values below 5 A are ignored, and n (which when treated as a free parameter has the value 2.53) is set to $\frac{5}{2}$, gives

$$F_P \approx \frac{1}{249}\frac{[B_{C2}(T, \varepsilon)]^{\frac{5}{2}}}{(2\pi\Phi_0)^{\frac{1}{2}}\mu_0\kappa^2(T, \varepsilon)}b^{\frac{1}{2}}(1-b)^2. \quad (13)$$

Both equations (12) and (13) provide expressions for F_p, which are dependent only on fundamental constants. For the data presented here, equation (12) is accurate to ±1 A at temperatures between 8 K and 14 K and at $\varepsilon = 0\%$, where it is possible to measure B_{C2} directly. At 4.2 K and 6 K the accuracy is reduced to ±4 A. For the Kramer parameterization given by

Table 8. The exponent of the flux pinning scaling law n, prefactor $G(\varepsilon)$ and T_C as a function of strain when B_{C2} is constrained at $5\%\rho_N$ and using a Kramer analysis for the Nb_3Al strand.

Strain, ε(%)	n	$G(\varepsilon)$ (10^{13} J^2 K^{-2} m^{-7})	T_C (K)
B_{C2} defined at $5\%\rho_N$			
−1.79	2.77	0.888	13.40
−1.47	2.67	1.14	13.84
−1.17	2.59	1.47	14.30
−0.89	2.57	1.63	14.67
−0.67	2.62	1.41	15.05
−0.45	2.60	1.45	15.31
−0.22	2.56	1.59	15.50
−0.11	2.58	1.52	15.59
0	2.58	1.51	15.63
0.11	2.58	1.51	15.64
0.22	2.57	1.59	15.61
0.33	2.60	1.47	15.59
0.45	2.55	1.65	15.50
0.56	2.57	1.56	15.43
0.67	2.60	1.41	15.35
B_{C2} defined from Kramer analysis			
−1.79	2.78	0.728	13.44
−1.47	2.60	1.13	13.83
−1.17	2.52	1.41	14.25
−0.89	2.81	0.708	14.82
−0.67	2.61	1.18	15.06
−0.45	2.56	1.38	15.29
−0.22	2.48	1.70	15.42
−0.11	2.48	2.15	15.49
0	2.47	2.19	15.51
0.11	2.47	2.22	15.52
0.22	2.47	2.25	15.51
0.33	2.47	2.18	15.48
0.45	2.46	2.27	15.41
0.56	2.45	2.20	15.36
0.67	2.44	2.26	15.24

equation (13), accuracy is further reduced to ±5 A at $\varepsilon = 0\%$ for the range 6 K $\leqslant T \leqslant$ 14 K. At 4.2 K the parameterization is less accurate probably because of the extrapolated B_{C2} data used and the commensurate uncertainty in κ data as can be seen in figure 28.

Figure 30 presents the RMS $I_C B$ error surface for all of the data in the temperature range 8 K $\leqslant T \leqslant$ 14 K as a function of p and q when B_{C2} is constrained at $5\%\rho_N$. The values of p and q used in the empirical fit are close to the minimum in the error surface as expected and show a larger uncertainty in p than q. The surface also shows that $p = 0.5$ and $q = 2$ (i.e. Kramer values) and $p = 1$, $q = 2.5$ can be considered for parameterizing data with less accuracy. In assuming half-integral values of p and q, comparison can be made with theoretical models [62]. In a different study, a limited set obtained at very high currents up to 2000 A as a function of field and temperature at zero strain have been obtained on the Nb_3Al strand [60]. The half-integral and optimum values of p and q suggested by figure 30 have been tested by plotting modified Kramer plots of the form $J_E^{\frac{1}{q}} B^{\frac{1-p}{q}}$ as a function of applied field which should yield approximate straight lines. Figure 31 shows these modified Kramer plots for (*a*) $p = 0.39$ and $q = 2.16$, (*b*) $p = 0.5$ and $q = 2$ and (*c*) $p = 1$ and $q = 2.5$. The modified Kramer plot for the optimized fit where $p = 0.39$ and $q = 2.16$

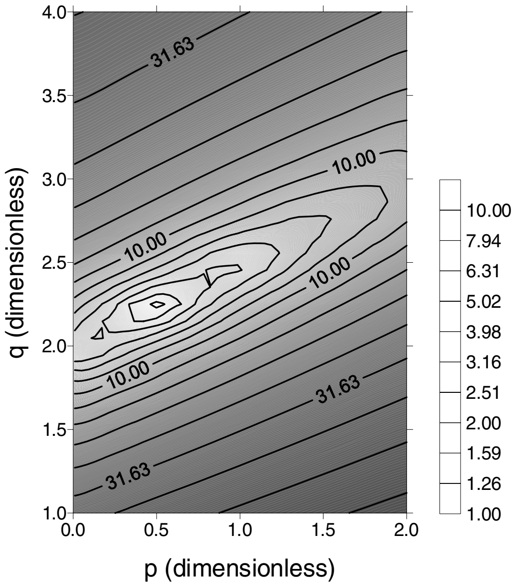

Figure 30. RMS $I_C B$ error surface plot as a function of p and q for all data in the temperature range 8 K $\leqslant T \leqslant$ 14 K for the Nb_3Al strand. The upper critical field in the fitting procedure was constrained at $5\%\rho_N$. The contours on the error surface plot are logarithmically spaced per decade as indicated on the legend.

and B_{C2} is constrained at $5\%\rho_N$ results in straight lines for all temperatures and all but the largest critical currents ($I_C \leqslant 1200$ A). A reasonable description is also found using the Kramer description where $p = 0.5$ and $q = 2$, although this is not as good as the optimized fit. However, for $p = 1$ and $q = 2.5$, there is a more noticeable curvature especially at high temperatures and high currents in the modified Kramer plot suggesting that these values are not acceptable for describing the data. In summary, the scaling behaviour of the limited data set up to high currents is consistent with the scaling of the comprehensive variable-strain variable-temperature presented in this work. Given a single scaling law, the fractional values of p and q provide the best fit to the data (equation (7)). Although the half-integral Kramer values provide a less-good parameterization it allows simple comparison with other measurements in the literature on Nb_3Al where it has been assumed that the Kramer functional form holds [29, 30, 38, 39].

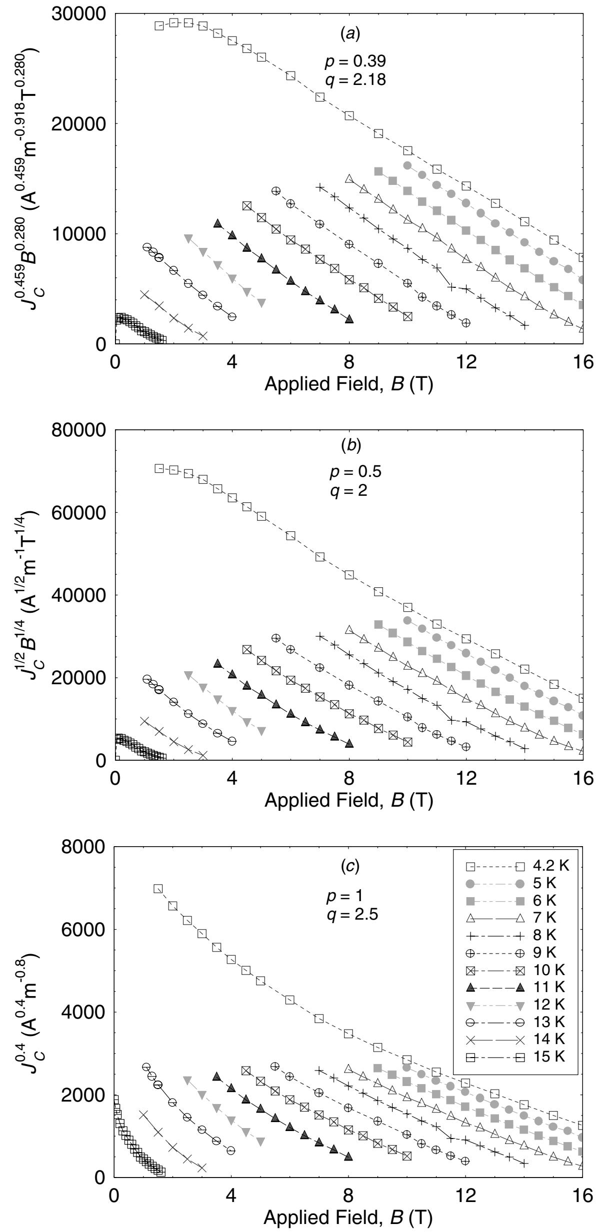

Figure 31. Modified Kramer plots, $J_E^{(\frac{1}{q})}B^{(\frac{1-p}{q})}$, as a function of magnetic field and temperature at $\varepsilon = 0\%$ for (*a*) $p = 0.39$ and $q = 2.16$, (*b*) $p = 0.5$ and $q = 2$ and (*c*) $p = 1$ and $q = 2.5$ for the Nb_3Al strand [59].

6. Discussion

There is an ongoing discussion about whether there is a significant strain gradient across the wire cross-section during compressive measurements using short bending springs [78, 79]. The resistivity measurements of upper critical field to $\varepsilon = -1.79\%$ (cf figures 11, 15 and 16) show positive and negative curvatures in compression, independently of the criterion used to define T_C and B_{C2} such that they cannot be described by an empirical power-law expression [16]. In general, the strain tolerance of B_{C2} is tensorial and dependent on the strain tolerance of the density of states, which is complex [36, 64, 80]. Nevertheless, we suggest that there are three aspects to the data that suggest that strain non-uniformity in the sample is not significant and that the data are representative of the strain values quoted: the resistive transition width for these data (see figure 10) was independent of strain for $-1\% \leqslant \varepsilon \leqslant 0.67\%$, and only increased slightly at higher strains when the spring was being plastically deformed to -1.79% from 1.0 T to ~1.1 T. The data obtained on all samples to date are consistent with free-standing axial tension measurements (see figure 12). Finally, the parameterization given by equation (7) holds throughout the entire strain–temperature phase space until B_{C2} is below about 2 T. Although it was not possible to check the reversibility of the strand after it was cycled to

-1.79%, these aspects of the data also suggest that the sample was not damaged during the entire experiment.

Previous measurements at zero strain on a powder-route Nb_3Al wire [63] have been parameterized by assuming p and q are the Kramer values and treating $T_C(\varepsilon)$ and $B_{C2}(T, \varepsilon)$ as fitting parameters. This gave $\nu = 1.5$. Measurements at zero strain on a high temperature reacted jelly-roll Nb_3Al wire [31], where B_{C2} was defined at $B_{C2}^{50\%\rho_N}(0, \varepsilon)$, gave values of $p = 0.52$, $q = 2.7$, $n = 3.73$ and $\nu = 1.4$. Measurements of J_E as a function of strain and temperature on a bronze route Nb_3Sn conductor [8] made in high fields until $J_E = 0$ (i.e. J_E is parameterized into the tail of the $J_E(B)$ characteristic) gave $p = 0.5$, $q = 3.5$, $n = 3.1$ and $\nu = 1.5$. These sets of values are consistent with the higher values for ν found for the technological fit in table 1 compared to those derived from direct resistivity measurements in table 5 and subsequent parameterization (equations (7), (12) and (13)) where $B_{C2}(T, \varepsilon)$ is defined near the onset of zero resistance from the resistivity data. Indeed, we note a general trend, consistent with table 5, that ν increases as the resistive criterion for B_{C2} increases either when measured directly or indirectly imposed through the parameterization. Equation (2) can be differentiated to give [8]

$$B_{C2}(0, \varepsilon) = -\frac{1}{\nu}\, T_C(\varepsilon) \frac{\partial B_{C2}(T, \varepsilon)}{\partial T}\bigg|_{T_C}. \qquad (14)$$

The experimental results presented here give $1/\nu \approx 0.8$ which is similar to the simple metal value of 0.69 [81] and consistent with the work which includes the effects of paramagnetic limiting and spin–orbit coupling [82, 83].

For idealized materials with a sharp distribution in B_{C2}, making measurements in sufficiently high magnetic fields until J_E is zero (i.e. in the tail up to B_{C2}) would be the natural way to identify B_{C2} and the scaling law. However, for the inhomogeneous Nb_3Al in this work, such an approach leads to values for $B_{C2}(T, \varepsilon)$ close to those at $95\%\rho_N$. This paper has demonstrated that scaling breaks down and p and q are strong functions of temperature (and strain) when the upper critical field is defined at $B_{C2}^{50\%\rho_N}$ and $B_{C2}^{95\%\rho_N}$ (see figures 19(*b*), (*c*) and 20(*b*), (*c*)). Necessarily if one assumes that scaling operates and hence that p and q are constants, a parameterization that includes the tail of J_E can only be an averaged value of this strong temperature dependence. Furthermore, if there is a broad distribution in B_{C2}, and J_E is parameterized in the tail, this tends to increase the value of q [84]. In summary, if the J_E data are parameterized in the tail of the distribution, the advantage of accurate parameterization at the highest fields must be offset against the correlations between the fitting parameters (see figure 18) causing p, q and ν to be increased and the break-down of accurate scaling.

The issue of how to identify a characteristic or average value for B_{C2} of the bulk of the Nb_3Al is a primary problem in accurately identifying the constants p and q in the Fietz–Webb scaling law. The approach of Kroeger *et al* has been adopted to find B_{C2} from resistivity measurements. Resistive measurements at high currents essentially map out more of the J_E surface. However, at sufficiently low currents, we have found that the shape of the resistivity transition is reasonably independent of sample current and so associates the width in the resistivity transition with the distribution in the upper critical field. In the limit that the width is independent of current one can also assume there are no flux creep effects [85, 86]. To a first approximation, one can rather simplistically interpret the onset of resistance $\left(\approx B_{C2}^{5\%\rho_N}(T, \varepsilon)\right)$ as an evidence for no percolative superconducting path. Theoretical work on percolative networks shows that in a two-dimensional system this occurs when about 40% of the material is normal [87, 88]. In three dimensions, 70–75% must be normal for there to be no percolative superconducting path and the resistive transition begins [88, 89]. Although these theoretical percentage values are dependent on how the connectivity of network is constructed, experimental support for these results has been observed in superconducting systems [90, 91]. Further information about compositional variations in Nb and Al both along and across the filament, the properties of the grain boundaries and the properties of the resistive state will be required to be more quantitative. Despite these uncertainties, given the good scaling we suggest $B_{C2}^{5\%\rho_N}(T, \varepsilon)$ is the relevant characteristic upper critical field in the scaling law at which a sizeable fraction of the Nb_3Al material is in both the superconducting and normal states.

From an engineering perspective where the most accurate description of J_E is required for all possible B–T–ε conditions, the technological fit provided is appropriate. For much of the temperature–strain phase space, this can be closely approximated by the empirical law (equation (7)) that self-consistently describes variable-temperature and variable-strain data as was found for Nb_3Sn [8]. Kroeger *et al* found very different results on their high bronze–niobium ratio monofilament to those reported here. The strain at which the peak in J_E and B_{C2} occurred differed by about 0.3%; the index n varied by about 25% and the prefactor $A(\varepsilon)$ varied by about a factor 3. In comparison, for the Nb_3Al reported here (and the Nb_3Sn multifilamentary conductor reported previously [8])—the peak in J_E and B_{C2} occurred at about the same strain, the variation in n as a function of strain is a few per cent and $A(\varepsilon)$ changes by $\sim$10% in the equivalent strain range. Further work would be required to determine to what degree these marked differences are due to the different materials investigated and/or due to the different sample current limits in which the resistivity data have been measured from which B_{C2} has then been extracted. If one assumes that a single mechanism determines J_E over the range of B–T–ε measured, then $p = 0.39$ and $q = 2.16$ provide the most accurate scaling. A Kramer analysis has also been completed where it is assumed that $p = 0.5$ and $q = 2$, which is less accurate but can be more easily compared to other results in the literature and theoretical work.

Experimental values of n for low-temperature type-II superconductors such as NbTi [75], V_3Ga [92], Nb_3Al [30], Nb_3Sn [35] and $PbMo_6S_8$ [66, 67, 93] are in the range $2 \leqslant n \leqslant 3$. Hence, the values of n obtained from constraining B_{C2} at $5\%\rho_N$ are consistent with both the theoretical [62] and experimental values in the literature. Equally, variable-strain measurements at 4.2 K on low-temperature superconductors gave $m = 1$, 1.2, 1.4, 1.6 and 4 for Nb_3Sn, Nb_3Sn with Hf and Ga additions, V_3Ga, Nb_3Ge and NbTi, respectively [94, 95]. There is a general trend that m increases as the sensitivity to strain of the normalized upper critical field decreases. This correlation is consistent with the increase in m from 0.86 to

2.14 for a Nb_3Sn conductor produced by an extra hot isostatic pressing reaction which also reduced the strain sensitivity of normalized B_{C2} [37] and the high value of m observed here for the Nb_3Al strand.

A complete description of the scaling law requires accurate knowledge of the prefactor $C(T, \varepsilon)$ in equation (1). Although the temperature and strain dependence of C has been measured and parameterized in terms of $A(\varepsilon)\left[B_{C2}^{5\%\rho_N}(T, \varepsilon)\right]^{2.18}$ (see equation (7)), all the work in the literature shows that the GL parameter must be included in any proper description of scaling. Since κ is not directly measured in transport measurements, we have used a GL relation to find a characteristic κ from the characteristic values of B_{C2} that were directly measured. The functional forms proposed (equations (12) and (13)) accurately describe both the magnitude and temperature dependence of J_E data at all strains as shown in figure 29 and are consistent with the zero-strain variable-temperature J_E data on $(NbTa)_3Sn$ [35]. The strain dependence is not explicitly confirmed because it is not possible from transport measurements alone to determine the strain dependence of κ. Nevertheless, agreement between the functional form and data is consistent with a reasonable strain dependence for the Sommerfeld constant (from which the strain dependence of κ can be calculated—equation (8)). The denominator in F_P given by equations (12) and (13) has a κ^2 term. If it is replaced by κ, one can only obtain agreement if the Sommerfeld constant, $\gamma(\varepsilon)$, increases as T_C decreases which is unphysical. If it is replaced by κ^3 (or higher powers), one has to postulate an unreasonably strong strain dependence for $\gamma(\varepsilon)$ so that an exponent value for κ of 2 is required. In this context, the difference between n and m in the prefactors for the scaling law (equations (3) and (4)) is attributed to the temperature and strain dependence of kappa. In the Kramer analysis which assumes that $p = 0.5$ and $q = 2$, the exponent of B_{C2} is close to 5/2 as observed in variable-temperature data on $(NbTa)_3Sn$ at zero strain [35].

An important feature of the functional form is that the primary multiplicative constant (i.e. 1/337 and 1/249 in equations (12) and (13) respectively) is dimensionless. It should be noted that ~80% of the non-Cu cross-sectional area of the strand becomes Nb_3Al. Therefore, the fraction of the entire cross-sectional area that is Nb_3Al is ~46%; so these multiplicative constants should be approximately doubled when considering the pinning in the superconducting layer alone. Simple dimensionality considerations imply that there is no requirement to add, for example, a constant grain size factor to the functional form. It is well established that in low fields, J_E is approximately inversely proportional to the grain size [96]. Nevertheless, Kramer pointed out in the 1970s that the high-field functional form of many superconductors approaches a limiting value that is well below (typically a few per cent [74] of) the depairing current [97, 98]. For example, comparison between Nb_3Sn material [99], or the Chevrel phase $SnMo_6S_8$ [100], with different grain sizes shows a clear saturation at the highest fields. There is no consensus explanation for saturation [74, 97, 98]. However, we conclude that in high fields, the parameterization that includes κ is most relevant for a comparison with theoretical work on the mechanism that determines J_E, and that the functional form of F_P suggests that J_E is not dependent on grain-size, consistent with J_E-microstructure correlations in other A15 and Chevrel phase superconducting materials.

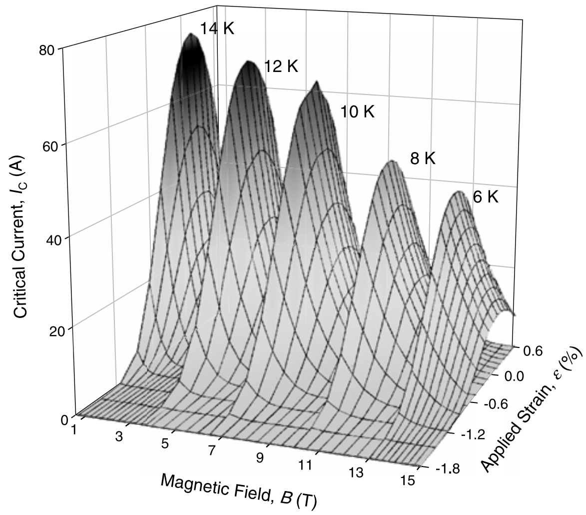

Figure 32. The four-dimensional critical current surface as a function of magnetic field, temperature and strain for the Nb_3Al strand.

7. Summary and conclusions

Detailed, accurate measurements of engineering critical current density and upper critical field have been made on a technological Nb_3Al conductor in magnetic fields up to 15 T, temperatures from 4.2 K up to the critical temperature and in the strain range from −1.79% to 0.67% as shown in figure 32. Improvements to the design of the probe have meant that the errors in the J_E measurements for temperatures above 4.2 K were equivalent to an uncertainty of ± 100 mK with a stability during the measurements of <5 mK. The limiting current at 4.2 K was 200 A and from 6 to 14 K was 80 A. The typical noise level on these measurements has been reduced to $\pm 1\ \mu V\ m^{-1}$ allowing J_E to be defined at $10\ \mu V\ m^{-1}$. These improvements have also allowed reliable measurements of the index of transition, N, throughout the temperature range. J_E was confirmed to be reversible at least over the strain range $-0.23\% < \varepsilon < 0.67\%$. Complementary resistivity measurements were taken to determine the upper critical field ($B_{C2}(T, \varepsilon)$) and the critical temperature ($T_C(\varepsilon)$) directly. At low currents the shape of the resistivity curve is only weakly dependent on the sample current. In this regime, when $B_{C2}(T, \varepsilon)$ is defined at $5\%\rho_N$, $50\%\rho_N$ or $95\%\rho_N$, an empirical relation is found where

$$B_{C2}^{\rho_N}(T, \varepsilon) = B_{C2}^{\rho_N}(0, \varepsilon)\left[1 - \left(\frac{T}{T_C^{\rho_N}(\varepsilon)}\right)^{\nu}\right] \qquad (15)$$

and an approximate relation $B_{C2}^{\rho_N}(0, \varepsilon) = 3.60 \times T_C^{\rho_N}(\varepsilon) - 29.86$ holds. The J_E data have been parameterized using the volume pinning force (F_P) where: $F_P = J_E \times B = A(\varepsilon)B_{C2}^{n}(T, \varepsilon)b^p(1-b)^q$ where $b = B/B_{C2}(T, \varepsilon)$. To achieve an accuracy of ~1 A, $B_{C2}(T, \varepsilon)$ was described by the empirical relation and three different ranges of temperature–strain were considered. The constants p, q, n and ν and the strain-dependent variables $A(\varepsilon)$, $B_{C2}(0, \varepsilon)$ and $T_C(\varepsilon)$ have been treated as free parameters and determined in each range.

When $B_{C2}(T, \varepsilon)$ is constrained to be the value at $50\%\rho_N$ or $95\%\rho_N$, the scaling law for F_P breaks down such that p and q are strong functions of temperature and q is also a strong function of strain. However, when $B_{C2}(T, \varepsilon)$ is defined at $5\%\rho_N$, there is good scaling where p and q are constants—independent of temperature and strain. If low J_E values in the high-field tail of the J_E–B relations are ignored, $\nu = 1.25$, $n = 2.18$, $p = 0.39$ and $q = 2.16$. Good scaling implies that $B_{C2}^{5\%\rho_N}(T, \varepsilon)$ provides the characteristic (or average) upper critical field of the bulk material although J_E is non-zero above $B_{C2}^{5\%\rho_N}(T, \varepsilon)$ and the current flow is percolative.

F_P can also be approximated by a form that explicitly includes the Ginzburg–Landau parameter, κ, given by

$$F_P = \frac{1}{337} \frac{\left[B_{C2}^{5\%\rho_N}(T, \varepsilon)\right]^{2.60}}{(2\pi\Phi_0)^{\frac{1}{2}}\mu_0\kappa^2(T, \varepsilon)} b^{0.39}(1-b)^{2.16} \qquad (12)$$

or a Kramer-like form

$$F_P = \frac{1}{249} \frac{[B_{C2}(T, \varepsilon)]^{\frac{5}{2}}}{(2\pi\Phi_0)^{\frac{1}{2}}\mu_0\kappa^2(T, \varepsilon)} b^{\frac{1}{2}}(1-b)^2, \qquad (13)$$

where

$$\kappa(T, \varepsilon) = \frac{B_{C2}(T, \varepsilon)}{\sqrt{2}B_C(T, \varepsilon)} = 924 \frac{B_{C2}(T, \varepsilon)}{\gamma^{\frac{1}{2}}(\varepsilon)T_C(\varepsilon)[1 - t^2]}, \qquad (8)$$

γ is the Sommerfeld constant and $t = T/T_C(\varepsilon)$. Since J_E is described using a scaling law that incorporates fundamental constants alone, it suggests that in high fields J_E is not dependent on grain-size, consistent with J_E-microstructure correlations in other superconducting materials.

Acknowledgments

The authors wish to thank P Foley and D Taylor in Durham, Dr C Forty at UKAEA, Drs H Fillunger and E Salpietro at EFDA and Dr N Mitchell at ITER. We acknowledge support from EPSRC (AF/100409) and from JAERI for supplying the Nb_3Al strands within the framework of ITER-EFDA [00-515].

References

[1] Iijima Y, Kikuchi A and Inoue K 2000 *Cryogenics* **40** 345–8
[2] Kikuchi A, Iijima Y, Inoue K, Kosuge M and Itoh K 2001 *IEEE Trans. Appl. Supercond.* **11** 3984–7
[3] Takeuchi T 2000 *Supercond. Sci. Technol.* **13** R101–19
[4] Takeuchi T, Banno N, Fukuzaki T and Wada H 2000 *Supercond. Sci. Technol.* **13** L11–14
[5] Glowacki B A 1999 *Intermetallics* **7** 117–40
[6] Kuroda T, Wada H, Iijima Y and Inoue K 1989 *J. Appl. Phys.* **65** 4445–7
[7] Cheggour N and Hampshire D P 1999 *J. Appl. Phys.* **86** 552–5
[8] Cheggour N and Hampshire D P 2002 *Cryogenics* at press
[9] Zeritis D, Ando T, Takahashi Y, Nishi M, Nakajima H and Shimamoto S 1990 *Appl. Phys. Lett.* **57** 506–7
[10] Specking W, Ando T, Tsuji H, Mikumo A and Yamada Y 1996 *Proc. 16th Int. Cryogenic Engineering Conf.* pp 1661–4
[11] Takeuchi T, Iijima Y, Inoue K, Wada H, ten Haken B, ten Kate H H J, Fukuda K, Iwaki G, Sakai S and Moriai H 1997 *Appl. Phys. Lett.* **71** 122–4
[12] Weber H W 1998 *Handbook of Applied Superconductivity* ed B Seeber (Bristol: Institute of Physics Publishing) pp 573–600
[13] Yamada Y *et al* 1999 *Cryogenics* **39** 115–22
[14] Koizumi N, Takahashi Y, Nunoya Y, Matsui K, Ando T, Tsuji H, Okuno K, Azuma K, Fuchs A and Bruzzone Vecsey G 2002 *Cryogenics* at press
[15] Koizumi N, Ando T, Sugimoto M, Takahashi Y, Tsuji H, Shimamoto S, Yamada Y, Mikumo A and Ayai N 1998 *Fusion Eng. Des.* **41** 277–81
[16] Ekin J W 1980 *Cryogenics* **20** 611–24
[17] Ekin J W, Fickett F R and Clark A F 1975 *Adv. Cryog. Eng.* **22** 449–52
[18] Ekin J W 1977 *IEEE Trans. Magn.* **13** 127–30
[19] Ekin J W, Yamashita T and Hamasaki K 1985 *IEEE Trans. Magn.* **21** 474–7
[20] Goldacker W, Specking W, Weiss F, Rimikis G and Flükiger R 1989 *Cryogenics* **29** 955–60
[21] Thieme C L H, Fleshler S, Buczek D M, Jowett M, Fritzmeier L G, Arendt P N, Foltyn S R, Coulter J Y and Willis J O 1999 *IEEE Trans. Appl. Supercond.* **9** 1494–7
[22] Ekin J W, Finnemore D K, Li Q, Tenbrink J and Carter W 1992 *Appl. Phys. Lett.* **61** 858–60
[23] Goldacker W, Keßler J, Ullmann B, Mossang E and Rikel M 1995 *IEEE Trans. Appl. Supercond.* **5** 1834–7
[24] Richens P E, Jones H, van Cleemput M and Hampshire D P 1997 *IEEE Trans. Appl. Supercond.* **7** 1315–8
[25] Hamid H A and Hampshire D P 1998 *Cryogenics* **38** 1007–15
[26] Kroeger D M, Easton D S, DasGupta A, Koch C C and Scarbrough J O 1980 *J. Appl. Phys.* **51** 2184–92
[27] ten Haken B, Godeke A and ten Kate H H J 1999 *J. Appl. Phys.* **85** 3247–53
[28] Godeke A, Krooshoop H J G, Knoopers H G, ten Haken B and ten Kate H H J 2001 *IEEE Trans. Appl. Supercond.* **11** 1526–9
[29] Ando T, Nunoya Y, Koizumi N, Sugimoto M, Tsuji H, Sato K and Yamada Y 1997 *IEEE Trans. Appl. Supercond.* **7** 1568–71
[30] Kuroda T, Murakami Y, Itoh K, Yuyama M, Wada H and Mao D 1998 *Cryogenics* **38** 785–9
[31] Banno N, Takeuchi T, Tagawa K, Itoh K, Wada H and Nakagawa K 2000 *IEEE Trans. Appl. Supercond.* **10** 1026–9
[32] Fietz W A and Webb W W 1969 *Phys. Rev.* **178** 657–67
[33] Tinkham M 1996 *Introduction to Superconductivity* 2nd edn (New York: McGraw-Hill)
[34] Kramer E J 1973 *J. Appl. Phys.* **44** 1360–70
[35] Hampshire D P, Jones H and Mitchell E W J 1985 *IEEE Trans. Magn.* **21** 289–92
[36] ten Haken B 1994 *PhD Thesis* Technical University of Twente
[37] Keys S A, Cheggour N and Hampshire D P 1999 *IEEE Trans. Appl. Supercond.* **9** 1447–50
[38] Itoh K, Kuroda T, Yuyama M, Iijima Y, Wada H, Murakami Y and Mao D 1997 *IEEE Trans. Appl. Supercond.* **7** 1576–9
[39] Mao D, Itoh K, Kuroda T, Yuyama M, Wada H and Murakami Y 1998 *Physica* C **301** 272–6
[40] Walters C R, Davidson I M and Tuck G E 1986 *Cryogenics* **26** 406–12
[41] Specking W, Nyilas A, Klemm M, Kling A and Flükiger R 1989 *Proc. 11th Conf. on Magnet Technology* pp 1009–14
[42] Ayai N *et al* 1999 *IEEE Trans. Appl. Supercond.* **9** 2688–91
[43] Cheggour N and Hampshire D P 2000 *Rev. Sci. Instrum.* **71** 4521–30

[44] Taylor D M J, Keys S A and Hampshire D P 2002 *Physica* C at press
[45] Keys S A and Hampshire D P 2002 *Handbook of Superconducting Materials* ed D Ginley and D Cardwell (Bristol: Institute of Physics Publishing) at press
[46] Goodrich L F and Fickett F R 1982 *Cryogenics* **22** 225–41
[47] Ekin J W 1989 *Appl. Phys. Lett.* **55** 905–7
[48] Seeber B 2001 Private communication
[49] Taylor D M J and Hampshire D P 2002 *J. Appl. Phys.* at press
[50] Mathu F and Meijer H C 1982 *Cryogenics* **22** 428
[51] Friend C M and Hampshire D P 1995 *Meas. Sci. Technol.* **6** 98–106
[52] Herrmann P F 1998 *Handbook of Applied Superconductivity* ed B Seeber (Bristol: Institute of Physics Publishing) pp 801–43
[53] Brandt B L, Liu D W and Rubin L G 1999 *Rev. Sci. Instrum.* **70** 104–10
[54] Ramsbottom H D, Ali S and Hampshire D P 1996 *Cryogenics* **36** 61–3
[55] Heine G and Lang W 1998 *Cryogenics* **38** 377–9
[56] Goodrich L F, Vecchia D F, Pittman E S, Ekin J W and Clark A F 1984 *NBS Special Publication* 1–53
[57] Ochiai O, Osamura K and Watanabe K 1993 *J. Appl. Phys.* **74** 440–5
[58] Hampshire D P and Jones H 1987 *Cryogenics* **27** 608–16
[59] ten Haken B, Godeke A, ten Kate H H J and Specking W 1996 *IEEE Trans. Magn.* **32** 2739–42
[60] Takahashi Y, Koizumi N, Nonuoya Y and Takaya Y *IEEE Trans. Appl. Supercond.* at press
[61] Campbell A M and Evetts J E 1972 *Adv. Phys.* **21** 199–428
[62] Dew-Hughes D 1974 *Phil. Magn.* **30** 293–305
[63] Cicchelli O, Bottura L, Gilson P and Spadoni M 1995 *IEEE Trans. Appl. Supercond.* **5** 901–4
[64] Godeke A, ten Haken B and ten Kate H H J 2002 *Physica* C at press
[65] Taylor D M J, Keys S A and Hampshire D P 2002 *Cryogenics* at press
[66] Zheng D N, Ramsbottom H D and Hampshire D P 1995 *Phys. Rev.* B **52** 12931–8
[67] Ramsbottom H D and Hampshire D P 1999 *J. Appl. Phys.* **85** 3732–9
[68] Wilson M 1998 *Superconducting Magnets* (Oxford: Oxford University Press)
[69] Kuroda T, Itoh K, Wada H and Togano K 2000 *Cryogenics* **40** 287–94
[70] Jeffery A 1992 *Mathematics for Engineers and Scientists* 4th edn (London: Chapman and Hall)
[71] Willens R H, Geballe T H, Gossard A C, Maita J P, Menth A, Hull G W Jr and Soden R R 1969 *Solid State Commun.* **7** 837–41
[72] Knapp G S, Bader S D and Fisk Z 1976 *Phys. Rev.* B **13** 3783–9
[73] Kwo J, Orlando T P and Beasley M R 1981 *Phys. Rev.* B **24** 2506–14
[74] Hampshire D P 1998 *Physica* C **296** 153–66
[75] Friend C M 1994 *PhD Thesis* University of Durham
[76] Ohtsuka T and Takano N 1967 *J. Phys. Soc. Japan* **23** 983–98
[77] Lim K C, Thompson J D and Webb G W 1983 *Phys. Rev.* B **27** 2781–7
[78] Ekin J W and Bray S L 1996 *Adv. Cryog. Eng.* **42** 1407–14
[79] ten Haken B, Godeke A and ten Kate H H J 1995 *IEEE Trans. Appl. Supercond.* **5** 1909–12
[80] Welch D O 1980 *Adv. Cryog. Eng.* **26** 48–65
[81] Hake R R 1967 *Phys. Rev.* **158** 356–76
[82] Werthamer N R, Helfand E and Hohenberg P C 1966 *Phys. Rev.* **147** 295–302
[83] Maki K 1966 *Phys. Rev.* **148** 362–9
[84] Wördenweber R 1999 *Rep. Prog. Phys.* **62** 187–236
[85] Sun J Z, Eom C B, Lairson B, Bravman J C and Geballe T H 1991 *Phys. Rev.* B **43** 3002–8
[86] Yeshurun Y and Malozemoff A P 1988 *Phys. Rev. Lett.* **60** 2202–5
[87] Zallen R 1983 *The Physics of Amorphous Solids* (New York: Wiley)
[88] Lorenz C D and Ziff R M 2001 *J. Chem. Phys.* **114** 3659–61
[89] Gingold D B and Lobb C J 1990 *Phys. Rev.* B **42** 8220–4
[90] Lobb C J, Tinkham M and Skocpol W J 1978 *Solid State Commun.* **27** 1273–5
[91] Harris D C, Herbert S T, Stroud D and Garland J C 1991 *Phys. Rev. Lett.* **67** 3606–9
[92] Hampshire D P, Clark A F and Jones H 1989 *J. Appl. Phys.* **66** 3160–7
[93] Cheggour N, Decroux M, Fischer Ø and Hampshire D P 1998 *J. Appl. Phys.* **84** 2181–3
[94] Ekin J W 1981 *IEEE Trans. Magn.* **17** 658–61
[95] Ekin J W 1984 *Adv. Cryog. Eng.* **30** 823–36
[96] Schauer W and Schelb W 1981 *IEEE Trans. Magn.* **17** 374–7
[97] Kramer E J 1975 *Electron. Mater.* **4** 839–80
[98] Osborne K E and Kramer E J 1974 *Phil. Mag.* **29** 685–94
[99] Enstrom R E and Appert J R 1973 *J. Appl. Phys.* **43** 1915–23
[100] Bonney L A, Willis T C and Larbalestier D C 1995 *J. Appl. Phys.* **77** 6377–87